

Higher-order surface FEM for incompressible Navier-Stokes flows on manifolds

T.P. Fries

March 28, 2018

Institute of Structural Analysis
Graz University of Technology
Lessingstr. 25/II, 8010 Graz, Austria

www.ifb.tugraz.at

fries@tugraz.at

Abstract

Stationary and instationary Stokes and Navier-Stokes flows are considered on two-dimensional manifolds, i.e., on curved surfaces in three dimensions. The higher-order surface FEM is used for the approximation of the geometry, velocities, pressure, and Lagrange multiplier to enforce tangential velocities. Individual element orders are employed for these various fields. Stream-line upwind stabilization is employed for flows at high Reynolds numbers. Applications are presented which extend classical benchmark test cases from flat domains to general manifolds. Highly accurate solutions are obtained and higher-order convergence rates are confirmed.

Keywords: Stokes, Navier-Stokes, higher-order FEM, surface FEM, surface PDEs, manifold

Contents

1	Introduction	4
2	Preliminaries	6
2.1	Surfaces	6
2.2	Surface operators	7
2.2.1	The tangential projector	7
2.2.2	Surface gradient of scalar quantities	7
2.2.3	Surface gradient of vector quantities	8
2.2.4	Divergence operators and divergence theorem	8
3	Governing equations	9
3.1	Flow models in strong form	9
3.1.1	Stationary Stokes flow	9
3.1.2	Stationary Navier-Stokes flow	11
3.1.3	Instationary Navier-Stokes flow	11
3.2	Flow models in weak form	12
3.2.1	Stationary Stokes flow	12
3.2.2	Stationary Navier-Stokes flow	13
3.2.3	Instationary Navier-Stokes flow	13
3.3	Surface FEM for flows on manifolds	14
3.3.1	Surface meshes	14
3.3.2	Surface FEM	15
3.3.3	Stationary Stokes flow	16
3.3.4	Stationary Navier-Stokes flow	17
3.3.5	Instationary Navier-Stokes flow	18

4	Numerical results	19
4.1	Stokes flow on an axisymmetric surface	20
4.2	Driven cavity flows on manifolds	25
4.3	Flows on zero-level sets	28
4.4	Cylinder flows	33
5	Conclusions	36
6	Acknowledgements	39
	References	39

1 Introduction

The solution of boundary value problems on curved surfaces has many practical applications in mathematics, physics, and engineering. For example, there are transport processes on interfaces, e.g., in foams, biomembranes and bubble surfaces [16, 25, 45], or structure-related phenomena such as in membranes and shells [2, 7]. Herein, Stokes and incompressible Navier-Stokes flows on curved, two-dimensional manifolds are considered. The governing equations for flows on *moving* surfaces are discussed in [3, 33] based on fundamental surface continuum mechanics and conservation laws and in [35], an energetic approach is presented. Earlier works in a similar context may be traced back to [15, 26, 43, 47]. For an excellent overview, the reader is referred to [33]. The references given above often focus on mathematical properties such as the existence and uniqueness of the solutions or stability analyses. Applications are often two-phase flows where the fluid field in the bulk and on the moving interface are coupled. However, it is also worthwhile to consider the situation for *fixed* manifolds, e.g., related to meteorology and oceanography where the flows take place on (part of) a sphere. Special geometries such as hyperbolic planes and spheres are discussed in [6, 34, 36].

Herein, the focus is on the approximation of stationary and instationary (Navier-)Stokes flows on fixed manifolds based on the surface finite element method as outlined in [11, 13, 14]. The governing equations resemble the three-dimensional (Navier-)Stokes equations where the classical gradient and divergence operators are replaced by their tangential counterparts derived from tangential differential calculus [33]. The equations are formulated in the classical stress-divergence form, contrasted to the approach in [37]. An additional constraint is required to enforce that the velocities remain in the tangent space of the manifold; it is labelled “tangential velocity constraint”. The models are first given in strong form and are then transformed to the weak form to enable a numerical solution based on the surface FEM. Finite element spaces of different orders are employed for the approximation of the geometry and of the involved physical fields, i.e., the velocities, pressure and the Lagrange multiplier field required to enforce the tangential velocity constraint. It is found that the balance of these element orders is critical for the accuracy and conditioning of the system of equations. In particular, the well-known Babuška-Brezzi condition applies [1, 4, 17] as both, the incompressibility constraint and the tangential velocity constraint are enforced using Lagrange multipliers. For the case of the instationary Navier-Stokes equations, the Crank-Nicolson time stepping scheme is employed for the semi-discrete system of equations

resulting from using the surface FEM in space. Surface FEM based on linear elements is used in the recent work [41], where the penalty method is employed to enforce tangential velocities and a projection method rather than a monolithic approach is suggested to solve for the different physical fields. Alternatives for the surface FEM are the TraceFEM [8, 22, 40] and CutFEM [27, 28], where the basis functions are generated from a background mesh in the bulk surrounding the manifold of interest.

Using the FEM for the Navier-Stokes flows at large Reynolds numbers requires stabilization. Herein, the streamline-upwind Petrov-Galerkin (SUPG) approach is used [5, 49]. Alternatively, other variants such as the Galerkin least squares stabilization [32] and variational multiscale approaches [29, 23] may also be employed. Stabilization for advection-diffusion applications on manifolds are considered in [38].

The numerical results show that higher-order convergence rates are achieved provided that the finite element spaces are properly chosen. Also the conditioning of the system of equations depends on the element orders employed for the approximation of the individual physical fields. The presented results are based on well-known benchmark test cases in two dimensions such as driven cavity flows and cylinder flows with vertex shedding which, herein, are extended to curved surfaces. Due to the higher-order elements, the results are highly accurate and may serve as future benchmarks in the context of (Navier-)Stokes flows on manifolds. Most test cases are carried out on parametrized surfaces, however, also the situation of flows on zero-isosurfaces is covered herein.

To the best of our knowledge, this is the first time, where (i) general higher-order surface FEM is used for the (in)stationary (Navier-)Stokes equations on manifolds including stabilization, (ii) numerical convergence studies are presented confirming higher-order convergence rates, and (iii) benchmark test cases are proposed and solutions presented. Furthermore the notation employed is closely related to the typical engineering literature and aims to provide a bridge from the mathematical to the engineering community.

The paper is organized as follows: In Section 2, some requirements and properties of surfaces are described and tangential differential operators are defined based on [10, 14]. Section 3 covers the governing equations for (i) Stokes flow, (ii) stationary, and (iii) instationary Navier-Stokes flows on two-dimensional manifolds. They are given in strong form, weak form, and discretized weak form according to the surface FEM. Numerical results are presented in Section 4. Convergence studies are performed for a test case for which an analytic solution is available and it is shown that higher-order convergence rates can be

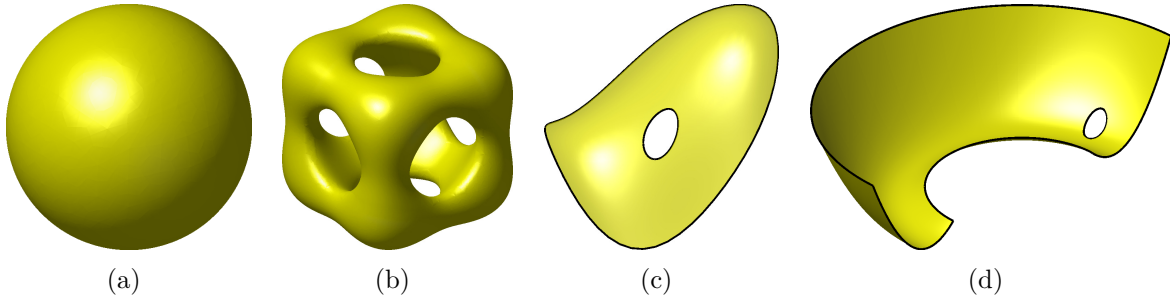


Figure 1: Some examples of (a, b) compact manifolds with $\partial\Gamma = \emptyset$ and (c, d) manifolds with boundary $\partial\Gamma$.

achieved. For the other test cases where no analytic solutions are available it is confirmed that in the flat two-dimensional case, well-known reference solutions are reproduced. Various meshes with different orders and resolutions have been employed to obtain highly accurate results on curved surfaces. Finally, a summary and outlook are given in Section 5.

2 Preliminaries

2.1 Surfaces

The task is to solve a boundary value problem (BVP) on an arbitrary surface Γ in three dimensions. Let the surface be fixed in space over time, possibly curved, sufficiently smooth, orientable, connected (so that there is only *one* surface), and feature a finite area. There is a unit normal vector $\mathbf{n}_\Gamma \in \mathbb{R}^3$ on Γ . The surface may be compact, i.e., without a boundary, $\partial\Gamma = \emptyset$, see Figs. 1(a) and (b) for examples. Otherwise, it may be bounded by $\partial\Gamma$ as shown in Figs. 1(c) and (d). Then, associated with $\partial\Gamma$, there is a tangential vector $\mathbf{t}_{\partial\Gamma}$ pointing in direction of $\partial\Gamma$ and a co-normal vector $\mathbf{n}_{\partial\Gamma} = \mathbf{n}_\Gamma \times \mathbf{t}_{\partial\Gamma}$ pointing “outwards” and being normal to $\partial\Gamma$ and tangent to Γ . The surface may be given in parametrized form or implied, e.g., based on the level-set method; both situations are considered herein. For the equivalence of these two cases and more mathematical details, see, e.g., [14].

2.2 Surface operators

2.2.1 The tangential projector

On the manifold Γ , the tangential projector $\mathbf{P}(\mathbf{x}) \in \mathbb{R}^{3 \times 3}$ is defined by the normal vector as

$$\mathbf{P}(\mathbf{x}) = \mathbf{I} - \mathbf{n}_\Gamma(\mathbf{x}) \otimes \mathbf{n}_\Gamma(\mathbf{x}).$$

Some important properties are: (i) $\mathbf{P} \cdot \mathbf{n}_\Gamma = \mathbf{0}$, (ii) $\mathbf{P} = \mathbf{P}^T$, and (iii) $\mathbf{P} \cdot \mathbf{P} = \mathbf{P}$.

2.2.2 Surface gradient of scalar quantities

The tangential gradient operator ∇_Γ of a differentiable scalar function $u : \Gamma \rightarrow \mathbb{R}$ on the manifold is given by

$$\nabla_\Gamma u(\mathbf{x}) = \mathbf{P}(\mathbf{x}) \cdot \nabla \tilde{u}(\mathbf{x}), \quad \mathbf{x} \in \Gamma, \quad (2.1)$$

where ∇ is the standard gradient operator, and \tilde{u} is a smooth extension of u in a neighborhood \mathcal{U} of the manifold Γ . Of course, \tilde{u} may also be some *given* function (rather than an arbitrary extension) in global coordinates, i.e., $\tilde{u}(\mathbf{x}) : \mathbb{R}^3 \rightarrow \mathbb{R}$. For the case of parametrized surfaces defined by the map $\mathbf{x}(\mathbf{r}) : \mathbb{R}^2 \rightarrow \mathbb{R}^3$, and a given scalar function $u(\mathbf{r}) : \mathbb{R}^2 \rightarrow \mathbb{R}$, the tangential gradient may be determined without explicitly computing an extension \tilde{u} using

$$\nabla_\Gamma u(\mathbf{x}(\mathbf{r})) = \mathbf{J}(\mathbf{r}) \cdot \mathbf{G}^{-1}(\mathbf{r}) \cdot \nabla_{\mathbf{r}} u(\mathbf{r}), \quad (2.2)$$

with $\mathbf{J} = \partial \mathbf{x} / \partial \mathbf{r}$ being the (3×2) -Jacobi matrix and $\mathbf{G} = \mathbf{J}^T \cdot \mathbf{J}$ being the metric tensor (first fundamental form). Equation (2.2) shall be used later in the context of the FEM to determine tangential gradients of shape functions. It is noteworthy that $\nabla_\Gamma u$ is in the tangent space of Γ and, thus, $\mathbf{P} \cdot \nabla_\Gamma u = \nabla_\Gamma u$ and $\nabla_\Gamma u \cdot \mathbf{n}_\Gamma = 0$. The components of the tangential gradient are denoted by

$$\nabla_\Gamma u(\mathbf{x}) = \left(\partial_x^\Gamma u, \partial_y^\Gamma u, \partial_z^\Gamma u \right)^\top,$$

representing the first-order partial derivatives on Γ . Second-order partial derivatives may be denoted by

$$\text{He}_{ij}(u(\mathbf{x})) = \partial_{x_i x_j}^\Gamma u(\mathbf{x}) = \partial_{x_i}^\Gamma \left(\partial_{x_j}^\Gamma u(\mathbf{x}) \right),$$

where $\text{He}_{ij}(u(\mathbf{x}))$ is the tangential Hessian matrix. In the context of manifolds, this matrix is not symmetric [10], i.e., for mixed second derivatives $\partial_{x_i x_j}^\Gamma u \neq \partial_{x_j x_i}^\Gamma u$ for $i \neq j$.

2.2.3 Surface gradient of vector quantities

Next, operators for vector quantities $\mathbf{u}(\mathbf{x}) : \Gamma \rightarrow \mathbb{R}^3$ are considered. The “directional gradient” of \mathbf{u} is the tensor of tangential derivatives and defined as

$$\nabla_\Gamma^{\text{dir}} \mathbf{u}(\mathbf{x}) = \nabla_\Gamma^{\text{dir}} \begin{bmatrix} u(\mathbf{x}) \\ v(\mathbf{x}) \\ w(\mathbf{x}) \end{bmatrix} = \begin{bmatrix} \partial_x^\Gamma u & \partial_y^\Gamma u & \partial_z^\Gamma u \\ \partial_x^\Gamma v & \partial_y^\Gamma v & \partial_z^\Gamma v \\ \partial_x^\Gamma w & \partial_y^\Gamma w & \partial_z^\Gamma w \end{bmatrix} = \nabla \tilde{\mathbf{u}} \cdot \mathbf{P}.$$

In contrast, the *covariant* derivatives are

$$\nabla_\Gamma^{\text{cov}} \mathbf{u}(\mathbf{x}) = \mathbf{P} \cdot \nabla_\Gamma^{\text{dir}} \mathbf{u}(\mathbf{x}) = \mathbf{P} \cdot \nabla \tilde{\mathbf{u}} \cdot \mathbf{P}.$$

One has to carefully distinguish these two different gradient operators. It is noted that $\nabla_\Gamma^{\text{cov}} \mathbf{u}$ appears frequently in the modeling of physical phenomena on manifolds, i.e., in the governing equations. On the other hand, $\nabla_\Gamma^{\text{dir}} \mathbf{u}$ is often used in straightforward extensions of identities such as product rules and divergence theorems. For example, we have for a scalar function $f(\mathbf{x})$ and vector functions $\mathbf{u}(\mathbf{x})$, $\mathbf{v}(\mathbf{x})$

$$\begin{aligned} \nabla_\Gamma^{\text{dir}} (f \cdot \mathbf{u}) &= \nabla_\Gamma f \otimes \mathbf{u} + f \cdot \nabla_\Gamma^{\text{dir}} \mathbf{u}, \\ \mathbf{v}^\text{T} \cdot \nabla_\Gamma^{\text{dir}} \mathbf{u} &= -\mathbf{u}^\text{T} \cdot \nabla_\Gamma^{\text{dir}} \mathbf{v} + \nabla_\Gamma^\text{T} (\mathbf{u} \cdot \mathbf{v}), \end{aligned}$$

however, the relations are less straightforward for the covariant counterparts $\nabla_\Gamma^{\text{cov}} (f \cdot \mathbf{u})$ and $\mathbf{v}^\text{T} \cdot \nabla_\Gamma^{\text{cov}} \mathbf{u}$, respectively. Later on, in the context of FEM implementations, it proves useful to transform covariant derivatives systematically to directional ones. This allows the computation of directional derivatives of FE shape functions with respect to $\mathbf{x} \in \mathbb{R}^3$ independent of the integration of the weak form of the governing equations.

2.2.4 Divergence operators and divergence theorem

The divergence of a vector function $\mathbf{u}(\mathbf{x}) : \Gamma \rightarrow \mathbb{R}^3$ is given as

$$\text{div}_\Gamma \mathbf{u}(\mathbf{x}) = \text{tr} \left(\nabla_\Gamma^{\text{dir}} \mathbf{u} \right) = \text{tr} \left(\nabla_\Gamma^{\text{cov}} \mathbf{u} \right) =: \nabla_\Gamma \cdot \mathbf{u}.$$

For a tensor function $\mathbf{A}(\mathbf{x}) : \Gamma \rightarrow \mathbb{R}^{3 \times 3}$, there holds

$$\operatorname{div}_\Gamma \mathbf{A}(\mathbf{x}) = \begin{bmatrix} \operatorname{div}_\Gamma(A_{11}, A_{12}, A_{13}) \\ \operatorname{div}_\Gamma(A_{21}, A_{22}, A_{23}) \\ \operatorname{div}_\Gamma(A_{31}, A_{32}, A_{33}) \end{bmatrix} =: \nabla_\Gamma \cdot \mathbf{A}.$$

It may be shown that $\operatorname{div}_\Gamma \mathbf{P} = -\varkappa \cdot \mathbf{n}_\Gamma$ with $\varkappa = \operatorname{tr}(\mathbf{H})$ being the mean curvature and $\mathbf{H} = \nabla_\Gamma^{\operatorname{cov}} \mathbf{n}_\Gamma$ being the second fundamental form.

The following divergence theorem on manifolds is later needed for deriving the weak forms [9, 10],

$$\int_\Gamma \mathbf{u} \cdot \operatorname{div}_\Gamma \mathbf{A} \, dA = - \int_\Gamma \nabla_\Gamma^{\operatorname{dir}} \mathbf{u} : \mathbf{A} \, dA + \int_\Gamma \varkappa \cdot \mathbf{u} \cdot \mathbf{A} \cdot \mathbf{n}_\Gamma \, dA + \int_{\partial\Gamma} \mathbf{u} \cdot \mathbf{A} \cdot \mathbf{n}_{\partial\Gamma} \, ds, \quad (2.3)$$

where $\nabla_\Gamma^{\operatorname{dir}} \mathbf{u} : \mathbf{A} = \operatorname{tr}(\nabla_\Gamma^{\operatorname{dir}} \mathbf{u} \cdot \mathbf{A}^\top)$. For *tangential* tensor functions with $\mathbf{A} = \mathbf{P} \cdot \mathbf{A} \cdot \mathbf{P}$, the term involving the curvature \varkappa vanishes because then $\mathbf{A} \cdot \mathbf{n}_\Gamma = \mathbf{0}$. In this case, we also have $\nabla_\Gamma^{\operatorname{dir}} \mathbf{u} : \mathbf{A} = \nabla_\Gamma^{\operatorname{cov}} \mathbf{u} : \mathbf{A}$.

3 Governing equations

In the following, we consider (i) stationary Stokes flow, (ii) stationary Navier-Stokes flow, and (iii) instationary Navier-Stokes flow on fixed manifolds. The governing equations are first given in strong and weak forms. The surface FEM is then applied for the discretization of the weak forms. As mentioned above, these models are also considered, e.g., in [3, 33, 35] among others.

3.1 Flow models in strong form

3.1.1 Stationary Stokes flow

Starting point is stationary Stokes flow on a manifold. Let $\mathbf{u}(\mathbf{x}) \in C^2(\Gamma)$ be the three-dimensional velocity field on the surface Γ , $p(\mathbf{x}) \in C^1(\Gamma)$ a pressure field, and $\mathbf{f}_t(\mathbf{x})$ a tangential body force, e.g., with unit N/m^2 . The governing field equations (in stress-

divergence-form [12]) to be fulfilled $\forall \mathbf{x} \in \Gamma$ are

$$-\mathbf{P} \cdot \operatorname{div}_\Gamma \boldsymbol{\sigma}(\mathbf{u}, p) = \mathbf{f}_t, \quad (3.1)$$

$$\operatorname{div}_\Gamma \mathbf{u} = 0, \quad (3.2)$$

$$\mathbf{u} \cdot \mathbf{n}_\Gamma = 0. \quad (3.3)$$

Equation (3.1) expands to three momentum equations, equation (3.2) is the incompressibility constraint and equation (3.3) represents the tangential velocity constraint that restricts the velocities to the tangent space of Γ . Two different strain tensors are introduced,

$$\boldsymbol{\varepsilon}^{\operatorname{dir}}(\mathbf{u}) = \frac{1}{2} \cdot \left(\nabla_\Gamma^{\operatorname{dir}} \mathbf{u} + \left(\nabla_\Gamma^{\operatorname{dir}} \mathbf{u} \right)^\top \right), \quad (3.4)$$

$$\boldsymbol{\varepsilon}^{\operatorname{cov}}(\mathbf{u}) = \frac{1}{2} \cdot \left(\nabla_\Gamma^{\operatorname{cov}} \mathbf{u} + \left(\nabla_\Gamma^{\operatorname{cov}} \mathbf{u} \right)^\top \right), \quad (3.5)$$

which are related to each other as $\boldsymbol{\varepsilon}^{\operatorname{cov}}(\mathbf{u}) = \mathbf{P} \cdot \boldsymbol{\varepsilon}^{\operatorname{dir}}(\mathbf{u}) \cdot \mathbf{P}$. The stress tensor is then defined as

$$\boldsymbol{\sigma}(\mathbf{u}, p) = -p \cdot \mathbf{P} + 2\mu \cdot \boldsymbol{\varepsilon}^{\operatorname{cov}}(\mathbf{u})$$

where $\mu \in \mathbb{R}^+$ is the (constant) dynamic viscosity. It is easily shown that

$$-\mathbf{P} \cdot \operatorname{div}_\Gamma \boldsymbol{\sigma}(\mathbf{u}, p) = \nabla_\Gamma p - 2\mu \mathbf{P} \cdot \operatorname{div}_\Gamma \boldsymbol{\varepsilon}^{\operatorname{cov}}(\mathbf{u})$$

Suppose there exists a boundary $\partial\Gamma$ of the manifold that consists of two non-overlapping parts, the Dirichlet boundary, $\partial\Gamma_{\operatorname{D}}$, and the Neumann boundary, $\partial\Gamma_{\operatorname{N}}$. The corresponding boundary conditions are given as

$$\begin{aligned} \mathbf{u}(\mathbf{x}) &= \hat{\mathbf{u}}(\mathbf{x}) && \text{on } \partial\Gamma_{\operatorname{D}}, \\ \boldsymbol{\sigma}(\mathbf{x}) \cdot \mathbf{n}_{\partial\Gamma}(\mathbf{x}) &= \hat{\mathbf{t}}(\mathbf{x}) && \text{on } \partial\Gamma_{\operatorname{N}}, \end{aligned} \quad (3.6)$$

where the prescribed velocities $\hat{\mathbf{u}}$ and tractions $\hat{\mathbf{t}}$ are in the tangent space of Γ , i.e., $\hat{\mathbf{u}} \cdot \mathbf{n}_\Gamma = \hat{\mathbf{t}} \cdot \mathbf{n}_\Gamma = 0$.

Note that, in general, there are no explicit boundary conditions needed for the pressure p . In cases where no Neumann boundary is present, i.e., $\partial\Gamma_{\operatorname{N}} = \emptyset$ and $\partial\Gamma_{\operatorname{D}} = \partial\Gamma$, the pressure is defined up to a constant [12, 24]. This includes compact manifolds where $\partial\Gamma = \emptyset$. In such situations, the pressure may be prescribed at a given point on Γ or it is imposed by a constraint in the form of $\int_\Gamma p \, dA = 0$.

Vorticity on manifolds. The vorticity $\boldsymbol{\omega}$ is a physical quantity frequently computed in flow problems. In the context of manifolds, we shall define

$$\boldsymbol{\omega} = \nabla_{\Gamma}^{\text{cov}} \times \mathbf{u}. \quad (3.7)$$

Note that $\boldsymbol{\omega}$ is co-linear to the normal vector \mathbf{n}_{Γ} , hence, $\mathbf{P} \cdot \boldsymbol{\omega} = \mathbf{0}$. Therefore, it is useful to determine the signed magnitude of $\boldsymbol{\omega}$, that is, the scalar function

$$\omega^*(\mathbf{x}) = \boldsymbol{\omega} \cdot \mathbf{n}_{\Gamma} = \pm \|\boldsymbol{\omega}\| \quad \forall \mathbf{x} \in \Gamma. \quad (3.8)$$

This scalar quantity may also be obtained using directional derivatives, i.e., $\omega^* = (\nabla_{\Gamma}^{\text{dir}} \times \mathbf{u}) \cdot \mathbf{n}_{\Gamma}$.

3.1.2 Stationary Navier-Stokes flow

For stationary *Navier-Stokes* flow, a non-linear advection term is added to equation (3.1) resulting into

$$\varrho \cdot (\mathbf{u} \cdot \nabla_{\Gamma}^{\text{cov}}) \mathbf{u} - \mathbf{P} \cdot \text{div}_{\Gamma} \boldsymbol{\sigma}(\mathbf{x}) = \mathbf{f}_t(\mathbf{x}), \quad (3.9)$$

where $\varrho \in \mathbb{R}^+$ is the (constant) fluid density with unit kg/m^3 and $(\mathbf{u} \cdot \nabla_{\Gamma}^{\text{cov}}) \mathbf{u} := (\nabla_{\Gamma}^{\text{cov}} \mathbf{u}) \cdot \mathbf{u}$. It is quite common to express the body force in the form $\mathbf{f}_t(\mathbf{x}) = \varrho \cdot \mathbf{g}_t(\mathbf{x})$ where \mathbf{g}_t may consider gravity as $\mathbf{g}_t = \mathbf{P} \cdot [0, 0, -9.81]^T \text{ m/s}^2$ for instance. The remaining equations (3.2) and (3.3) and the boundary conditions (3.6) remain unchanged. The solution of the non-linear governing equations can be obtained iteratively based on the Newton-Raphson method or other fixed-point iterations such as Picard iterations. Because the advection operator is not self-adjoint, well-known stability issues may arise for large Reynolds numbers in a numerical context.

3.1.3 Instationary Navier-Stokes flow

For *instationary* Navier-Stokes flow, the momentum equation (3.1) changes to

$$\varrho \cdot (\partial_t \mathbf{u}(\mathbf{x}, t) + (\mathbf{u} \cdot \nabla_{\Gamma}^{\text{cov}}) \mathbf{u} - \mathbf{g}_t(\mathbf{x}, t)) - \mathbf{P} \cdot \text{div}_{\Gamma} \boldsymbol{\sigma}(\mathbf{x}, t) = \mathbf{0}. \quad (3.10)$$

The functions representing the physical fields live in space (on Γ) and time, i.e., in the time interval $\tau = [0, T]$. Therefore, Eqs. (3.10), (3.2), and (3.3) have to be solved in the

space-time domain $\Gamma \times \tau$. Herein, we restrict ourselves to spatially fixed manifolds Γ .

The boundary conditions (3.6) also extend in time dimension, hence, there are prescribed velocities $\hat{\mathbf{u}}(\mathbf{x}, t)$ along $\partial\Gamma_D \times \tau$ and tractions $\hat{\mathbf{t}}(\mathbf{x}, t)$ along $\partial\Gamma_N \times \tau$. Furthermore, an initial condition is needed,

$$\mathbf{u}(\mathbf{x}, 0) = \mathbf{u}_0(\mathbf{x}), \text{ with } \operatorname{div}_\Gamma \mathbf{u}_0 = 0 \text{ and } \mathbf{u}_0 \cdot \mathbf{n}_\Gamma = 0 \quad \forall \mathbf{x} \in \Gamma \text{ at } t = 0. \quad (3.11)$$

3.2 Flow models in weak form

The following trial and test function spaces are introduced,

$$\mathcal{S}_u = \left\{ \mathbf{u} \in \mathcal{H}^1(\Gamma)^3, \mathbf{u} = \hat{\mathbf{u}} \text{ on } \partial\Gamma_D \right\}, \quad (3.12)$$

$$\mathcal{V}_u = \left\{ \mathbf{w}_u \in \mathcal{H}^1(\Gamma)^3, \mathbf{w}_u = \mathbf{0} \text{ on } \partial\Gamma_D \right\}, \quad (3.13)$$

$$\mathcal{S}_p = \mathcal{V}_p = \mathcal{L}_2(\Gamma), \quad (3.14)$$

$$\mathcal{S}_\lambda = \mathcal{V}_\lambda = \mathcal{L}_2(\Gamma). \quad (3.15)$$

As mentioned previously, if no Neumann boundary exists, i.e., $\partial\Gamma_N = \emptyset$, the pressure is defined up to a constant and one may replace \mathcal{S}_p by

$$\mathcal{S}_p^0 = \left\{ p \in \mathcal{L}_2(\Gamma), \int_\Gamma p \, dA = 0 \right\}.$$

3.2.1 Stationary Stokes flow

The weak form of the Stokes problem becomes: Given viscosity $\mu \in \mathbb{R}^+$, body force $\mathbf{f}(\mathbf{x})$ in Γ , and traction $\hat{\mathbf{t}}(\mathbf{x})$ on $\partial\Gamma_N$, find the velocity field $\mathbf{u}(\mathbf{x}) \in \mathcal{S}_u$, pressure field $p(\mathbf{x}) \in \mathcal{S}_p$, and Lagrange multiplier field $\lambda(\mathbf{x}) \in \mathcal{S}_\lambda$ such that for all test functions $(\mathbf{w}_u, w_p, w_\lambda) \in \mathcal{V}_u \times \mathcal{V}_p \times \mathcal{V}_\lambda$, there holds in Γ

$$\int_\Gamma \nabla_\Gamma^{\text{dir}} \mathbf{w}_u : \boldsymbol{\sigma}(\mathbf{u}, p) \, dA + \int_\Gamma \lambda \cdot (\mathbf{w}_u \cdot \mathbf{n}_\Gamma) \, dA = \int_\Gamma \mathbf{w}_u \cdot \mathbf{f} \, dA + \int_{\partial\Gamma_N} \mathbf{w}_u \cdot \hat{\mathbf{t}} \, ds, \quad (3.16)$$

$$\int_\Gamma w_p \cdot \operatorname{div}_\Gamma \mathbf{u} \, dA = 0, \quad (3.17)$$

$$\int_\Gamma w_\lambda \cdot (\mathbf{u} \cdot \mathbf{n}_\Gamma) \, dA = 0. \quad (3.18)$$

In order to obtain Eq. (3.16), the divergence theorem (2.3) was applied to $-\int_\Gamma \mathbf{w}_u \cdot \operatorname{div}_\Gamma \boldsymbol{\sigma} \, dA$ where the curvature term vanishes due to $\boldsymbol{\sigma} \cdot \mathbf{n}_\Gamma = \mathbf{0}$. Using the definition

of the stress tensor, we get

$$\int_{\Gamma} \nabla_{\Gamma}^{\text{dir}} \mathbf{w}_u : \boldsymbol{\sigma}(\mathbf{u}, p) \, dA = - \int_{\Gamma} \nabla_{\Gamma}^{\text{dir}} \mathbf{w}_u : (p \cdot \mathbf{P}) \, dA + 2\mu \cdot \int_{\Gamma} \nabla_{\Gamma}^{\text{dir}} \mathbf{w}_u : \boldsymbol{\varepsilon}^{\text{cov}}(\mathbf{u}) \, dA$$

The following relations are easily derived:

$$\begin{aligned} \nabla_{\Gamma}^{\text{dir}} \mathbf{w}_u : (p \cdot \mathbf{P}) &= p \cdot \text{tr}(\nabla_{\Gamma}^{\text{dir}} \mathbf{w}_u \cdot \mathbf{P}) \\ &= p \cdot \text{div}_{\Gamma} \mathbf{w}_u \\ \nabla_{\Gamma}^{\text{dir}} \mathbf{w}_u : \boldsymbol{\varepsilon}^{\text{cov}}(\mathbf{u}) &= \text{tr}(\nabla_{\Gamma}^{\text{dir}} \mathbf{w}_u \cdot \boldsymbol{\varepsilon}^{\text{cov}}(\mathbf{u})) \\ &= \text{tr}(\boldsymbol{\varepsilon}^{\text{cov}}(\mathbf{w}_u) \cdot \boldsymbol{\varepsilon}^{\text{cov}}(\mathbf{u})) \\ &= \text{tr}(\mathbf{P} \cdot \nabla_{\Gamma}^{\text{dir}} \mathbf{w}_u \cdot \boldsymbol{\varepsilon}^{\text{dir}}(\mathbf{u}) \cdot \mathbf{P}) \end{aligned} \quad (3.19)$$

It is readily verified that solutions of the strong form also fulfill the weak form from above. This is obvious for Eqs. (3.17) and (3.18) due to Eqs. (3.2) and (3.3), respectively. For the momentum equations, it is noted that (3.16) is fulfilled for $-\text{div}_{\Gamma} \boldsymbol{\sigma}(\mathbf{u}, p) + \lambda \cdot \mathbf{n}_{\Gamma} = \mathbf{f}$. Restricting this to the tangential space by multiplication with the projector \mathbf{P} yields the strong form of the momentum equations (3.1) because $\mathbf{P} \cdot \mathbf{n}_{\Gamma} = \mathbf{0}$. It is thus also seen that the Lagrange multiplier field λ may be physically interpreted as a force in normal direction.

3.2.2 Stationary Navier-Stokes flow

The weak form of the stationary Navier-Stokes equations is similar to the Stokes problem from above, however, Eq. (3.16) is replaced by

$$\begin{aligned} \rho \cdot \int_{\Gamma} \mathbf{w}_u \cdot (\mathbf{u} \cdot \nabla_{\Gamma}^{\text{cov}}) \mathbf{u} \, dA + \int_{\Gamma} \nabla_{\Gamma}^{\text{dir}} \mathbf{w}_u : \boldsymbol{\sigma}(\mathbf{u}, p) \, dA + \int_{\Gamma} \lambda \cdot (\mathbf{w}_u \cdot \mathbf{n}_{\Gamma}) \, dA \\ = \int_{\Gamma} \mathbf{w}_u \cdot \mathbf{f} \, dA + \int_{\partial\Gamma_{\text{N}}} \mathbf{w}_u \cdot \hat{\mathbf{t}} \, ds \end{aligned}$$

where the added advection term is readily identified.

3.2.3 Instationary Navier-Stokes flow

The weak form of the instationary Navier-Stokes problem is: Given density $\rho \in \mathbb{R}^+$, viscosity $\mu \in \mathbb{R}^+$, body force $\rho \cdot \mathbf{g}(\mathbf{x}, t)$ in $\Gamma \times \tau$, traction $\hat{\mathbf{t}}(\mathbf{x}, t)$ on $\partial\Gamma_{\text{N}} \times \tau$, and initial condition

$u_0(\mathbf{x})$ on Γ at $t = 0$ according to (3.11), find the velocity field $\mathbf{u}(\mathbf{x}, t) \in L_2(\tau; \mathcal{S}_u)$, pressure field $p(\mathbf{x}, t) \in L_2(\tau; \mathcal{S}_p)$, and Lagrange multiplier field $\lambda(\mathbf{x}, t) \in L_2(\tau; \mathcal{S}_\lambda)$ such that for all test functions $(\mathbf{w}_u, w_p, w_\lambda) \in \mathcal{V}_u \times \mathcal{V}_p \times \mathcal{V}_\lambda$, there holds in $\Gamma \times \tau$

$$\begin{aligned} & \varrho \cdot \int_{\Gamma} \mathbf{w}_u \cdot (\partial_t \mathbf{u} + (\mathbf{u} \cdot \nabla_{\Gamma}^{\text{cov}}) \mathbf{u} - \mathbf{g}) \, dA \\ & + \int_{\Gamma} \nabla_{\Gamma} \mathbf{w}_u^{\text{dir}} : \boldsymbol{\sigma}(\mathbf{u}, p) \, dA + \int_{\Gamma} \lambda \cdot (\mathbf{w}_u \cdot \mathbf{n}_{\Gamma}) \, dA = \int_{\partial\Gamma_N} \mathbf{w}_u \cdot \hat{\mathbf{t}} \, ds, \end{aligned} \quad (3.20)$$

$$\int_{\Gamma} w_p \cdot \text{div}_{\Gamma} \mathbf{u} \, dA = 0, \quad (3.21)$$

$$\int_{\Gamma} w_\lambda \cdot (\mathbf{u} \cdot \mathbf{n}_{\Gamma}) \, dA = 0. \quad (3.22)$$

3.3 Surface FEM for flows on manifolds

3.3.1 Surface meshes

Assume that a suitable surface mesh composed by higher-order triangular or quadrilateral Lagrange elements of order q may be generated with desired element sizes and all nodes on Γ . Well-known, necessary requirements of meshes such as the shape regularity of the elements and bounds on inner angles, are fulfilled. The shape of each (physical) element in the mesh results from a map of the corresponding reference element with n_q nodes,

$$\mathbf{x}(\mathbf{r}) = \begin{bmatrix} x(r, s) \\ y(r, s) \\ z(r, s) \end{bmatrix} = \sum_{i=1}^{n_q} N_i^q(\mathbf{r}) \mathbf{x}_i. \quad (3.23)$$

$N_i^q(\mathbf{r})$ are classical Lagrangean shape functions of order q in reference coordinates $\mathbf{r} \in \mathbb{R}^2$ and $\mathbf{x}_i \in \Gamma$ are the nodal coordinates. The resulting mesh is an approximation $\Gamma_q^h \in C^0$ of the exact surface Γ . Clearly, Γ_q^h is defined *parametrically* through the map (3.23) even if the original Γ was implicitly given, e.g., by the zero-isosurface of a level-set function. See [18, 19, 20] for the automatic generation of higher-order meshes on zero-isosurfaces. The discrete unit normal vector is

$$\mathbf{n}_{\Gamma}^h = \frac{\partial_r \mathbf{x} \times \partial_s \mathbf{x}}{\|\partial_r \mathbf{x} \times \partial_s \mathbf{x}\|}$$

and is not smooth across element edges due to the C^0 -continuity of the surface mesh. The discrete tangent and co-normal vectors $\mathbf{t}_{\partial\Gamma}^h$ and $\mathbf{n}_{\partial\Gamma}^h$ are easily obtained along the element edges on the boundary of Γ_q^h . The definitions of the surface operators from Section 2.2

readily extend to the case of a discrete manifold Γ_q^h and are not repeated here.

3.3.2 Surface FEM

We use higher-order surface FEM as detailed, e.g., in [11, 14] for the discretization of the weak forms from above. Finite element spaces of different orders are involved. As mentioned before, suitable surface meshes of order q may be generated defining approximations $\Gamma_q^h \in C^0$ of Γ . Let there be a “geometry mesh” of order $q = k_{\text{geom}}$ with the sole purpose to approximate the geometry of the manifold $\Gamma^h = \Gamma_{k_{\text{geom}}}^h$ and define the element maps (3.23). In particular, this mesh is not used to imply a finite element space for the approximation of the weak forms.

Next, a finite element space of order k is generated on Γ^h for which it is assumed that there is a second mesh of order k . The two meshes feature the same element types and number of elements with identical coordinates at the corners, however, the total number of nodes differs due to the individual orders. It is emphasized that the coordinates of the nodes in the k -th order mesh are, in fact, never needed and it is only the connectivity which is required to set up the finite element space.

Associated to triangular or quadrilateral elements in the k -th order mesh, there is a fixed set of *local* basis functions $\{N_i^k(\mathbf{r})\}$ defined in a reference element with $i = 1, \dots, n_k$ and n_k being the number of nodes per element. Classical Lagrange basis functions with $N_i^k(\mathbf{r}_j) = \delta_{ij}$ are used herein. Based on the map (3.23) which is completely determined by the geometry mesh, one may generate $\{N_i^k(\mathbf{x}(\mathbf{r}))\}$ for all $\mathbf{x} \in \Gamma^h$ and tangential derivatives $\nabla_{\Gamma} N_i^k(\mathbf{x}(\mathbf{r}))$ are determined based on Eq. (2.2). This is only an *iso*-parametric map when $k = k_{\text{geom}}$. Summing up the element contributions for nodes belonging to several elements, this generates a set of *global*, C^0 -continuous basis functions $\{M_i^k(\mathbf{x}(\mathbf{r}))\}$ in Γ^h with $i = 1, \dots, n_{\text{nodes}}^k$ and n_{nodes}^k being the number of nodes of the k -th order surface mesh. Note that to generate the nodal basis $\{M_i^k(\mathbf{x}(\mathbf{r}))\}$, only the coordinates of the geometry mesh are needed, however, not from the k -th order mesh. A general finite element space of order k is now defined by

$$\mathcal{Q}_k^h = \left\{ u^h \in C_0(\Gamma_{k_{\text{geom}}}^h), u^h = \sum_{i=1}^{n_{\text{nodes}}^k} M_i^k(\mathbf{x}(\mathbf{r})) \cdot u_i, u_i \in \mathbb{R} \right\} \subset \mathcal{H}^1(\Gamma_{k_{\text{geom}}}^h).$$

Based on this, the following discrete trial and test function spaces are defined,

$$\mathcal{S}_u^h = \left\{ \mathbf{u}^h \in [\mathcal{Q}_{k_u}^h]^3, \mathbf{u}^h = \hat{\mathbf{u}}^h \text{ on } \partial\Gamma_D^h \right\}, \quad (3.24)$$

$$\mathcal{V}_u^h = \left\{ \mathbf{w}_u^h \in [\mathcal{Q}_{k_u}^h]^3, \mathbf{w}_u^h = \mathbf{0} \text{ on } \partial\Gamma_D^h \right\}, \quad (3.25)$$

$$\mathcal{S}_p^h = \mathcal{V}_p^h = \mathcal{Q}_{k_p}^h, \quad (3.26)$$

$$\mathcal{S}_\lambda^h = \mathcal{V}_\lambda^h = \mathcal{Q}_{k_\lambda}^h. \quad (3.27)$$

Although shape functions for the pressure and the Lagrange multiplier for enforcing the tangential velocity constraint may be discontinuous, we restrict ourselves to classical C^0 -continuous approximations. Note that individual orders k_u , k_p , and k_λ are associated to the approximations of velocities \mathbf{u}^h , pressure p^h , and Lagrange multiplier field λ^h , respectively. Analogous to the continuous case, one may impose that the functions in \mathcal{S}_p^h have to fulfill $\int_\Gamma p^h dA = 0$ if no Neumann boundary is present.

3.3.3 Stationary Stokes flow

The discrete weak form of the Stokes problem reads: Given viscosity $\mu \in \mathbb{R}^+$, body force $\mathbf{f}^h(\mathbf{x})$ in Γ^h , and traction $\hat{\mathbf{t}}^h(\mathbf{x})$ on $\partial\Gamma_N^h$, find the velocity field $\mathbf{u}^h(\mathbf{x}) \in \mathcal{S}_u^h$, pressure field $p^h(\mathbf{x}) \in \mathcal{S}_p^h$, and Lagrange multiplier field $\lambda^h(\mathbf{x}) \in \mathcal{S}_\lambda^h$ such that for all test functions $(\mathbf{w}_u^h, w_p^h, w_\lambda^h) \in \mathcal{V}_u^h \times \mathcal{V}_p^h \times \mathcal{V}_\lambda^h$, there holds in Γ^h

$$\int_\Gamma \nabla_\Gamma^{\text{dir}} \mathbf{w}_u^h : \boldsymbol{\sigma}(\mathbf{u}^h, p^h) dA + \int_\Gamma \lambda^h \cdot (\mathbf{w}_u^h \cdot \mathbf{n}_\Gamma^h) dA = \int_\Gamma \mathbf{w}_u^h \cdot \mathbf{f}^h dA + \int_{\partial\Gamma_N^h} \mathbf{w}_u^h \cdot \hat{\mathbf{t}}^h dA, \quad (3.28)$$

$$\int_\Gamma w_p^h \cdot \text{div}_\Gamma \mathbf{u}^h dA = 0, \quad (3.29)$$

$$\int_\Gamma w_\lambda^h \cdot (\mathbf{u}^h \cdot \mathbf{n}_\Gamma^h) dA = 0. \quad (3.30)$$

The usual element assembly yields a linear system of equations in the form

$$\begin{bmatrix} \mathbf{K} & \mathbf{G} & \mathbf{L} \\ \mathbf{G}^T & \mathbf{0} & \mathbf{0} \\ \mathbf{L}^T & \mathbf{0} & \mathbf{0} \end{bmatrix} \cdot \begin{bmatrix} \underline{\mathbf{u}} \\ \mathbf{p} \\ \boldsymbol{\lambda} \end{bmatrix} = \begin{bmatrix} \mathbf{f} \\ \mathbf{0} \\ \mathbf{0} \end{bmatrix}, \quad (3.31)$$

with $[\underline{\mathbf{u}}, \mathbf{p}, \boldsymbol{\lambda}]^T = [\mathbf{u}, \mathbf{v}, \mathbf{w}, \mathbf{p}, \boldsymbol{\lambda}]^T$ being the sought nodal values of the velocity components, pressure, and Lagrange multiplier. For the implementation, it is interesting to compare the

system (3.31) with the system obtained for a classical three-dimensional Stokes problem,

$$\begin{bmatrix} \mathbf{K}_{3\text{D}} & \mathbf{G}_{3\text{D}} \\ \mathbf{G}_{3\text{D}}^T & \mathbf{0} \end{bmatrix} \cdot \begin{bmatrix} \mathbf{u} \\ p \end{bmatrix} = \begin{bmatrix} \mathbf{f} \\ \mathbf{0} \end{bmatrix}. \quad (3.32)$$

Assume a function which generates $\mathbf{K}_{3\text{D}}$ and $\mathbf{G}_{3\text{D}}$ based on three-dimensional FE shape functions (including classical partial derivatives with respect to \mathbf{x}) evaluated at given integration points in 3D. The same function may be used for generating \mathbf{K} and \mathbf{G} provided that (i) the integration points are restricted to Γ^h with proper weights, (ii) the classical partial derivatives in ∇ are replaced by the tangential derivatives as in $\nabla_{\Gamma}^{\text{dir}}$, and (iii) the contribution to \mathbf{K} at the current integration point, $\mathbf{K}(\mathbf{x}_i)$, is projected as $\mathbf{K}(\mathbf{x}_i) = \mathbf{P}(\mathbf{x}_i) \cdot \mathbf{K}_{3\text{D}}(\mathbf{x}_i) \cdot \mathbf{P}(\mathbf{x}_i)$ which is due to Eq. (3.19). The same shall later hold for the advection matrix $\mathbf{C}(\mathbf{u})$ in the Navier-Stokes equations.

As expected in the context of the Lagrange multiplier method, the matrix in Eq. (3.31) has a saddle-point structure and is typical for a mixed FEM. The well-known Babuška-Brezzi condition [1, 4, 17] must be fulfilled to obtain useful solutions for all involved fields. This may be achieved by adjusting the orders of the approximation spaces for the different fields and is further detailed in the numerical results. It is noted that stabilization may be employed to circumvent the Babuška-Brezzi condition rather than to fulfill it, see, e.g., [17, 30, 31] which is, however, beyond the scope of this work.

3.3.4 Stationary Navier-Stokes flow

The discrete weak form of the stationary Navier-Stokes problem reads: Given density $\varrho \in \mathbb{R}^+$, viscosity $\mu \in \mathbb{R}^+$, body force $\varrho \cdot \mathbf{g}^h(\mathbf{x})$ in Γ^h , and traction $\hat{\mathbf{t}}^h(\mathbf{x})$ on $\partial\Gamma_{\text{N}}^h$, find the velocity field $\mathbf{u}^h(\mathbf{x}) \in \mathcal{S}_u^h$, pressure field $p^h(\mathbf{x}) \in \mathcal{S}_p^h$, and Lagrange multiplier field $\lambda^h(\mathbf{x}) \in \mathcal{S}_\lambda^h$ such that for all test functions $(\mathbf{w}_u^h, w_p^h, w_\lambda^h) \in \mathcal{V}_u^h \times \mathcal{V}_p^h \times \mathcal{V}_\lambda^h$, there holds in Γ^h

$$\begin{aligned} & \varrho \cdot \int_{\Gamma} \mathbf{w}_u^h \cdot \left((\mathbf{u}^h \cdot \nabla_{\Gamma}^{\text{cov}}) \mathbf{u}^h - \mathbf{g}^h \right) dA + \int_{\Gamma} \nabla_{\Gamma}^{\text{dir}} \mathbf{w}_u^h : \boldsymbol{\sigma}(\mathbf{u}^h, p^h) dA + \int_{\Gamma} \lambda^h \cdot (\mathbf{w}_u^h \cdot \mathbf{n}_{\Gamma}^h) dA \\ & - \int_{\partial\Gamma_{\text{N}}} \mathbf{w}_u^h \cdot \hat{\mathbf{t}}^h ds + \int_{\Gamma} w_p^h \cdot \text{div}_{\Gamma} \mathbf{u}^h dA + \int_{\Gamma} w_\lambda^h \cdot (\mathbf{u}^h \cdot \mathbf{n}_{\Gamma}^h) dA \\ & + \sum_{e=1}^{n_{\text{el}}} \int_{\Gamma_e} \tau_{\text{SUPG}} \left((\mathbf{u}^h \cdot \nabla_{\Gamma}^{\text{cov}}) \mathbf{w}_u^h \right) \cdot \left[\varrho \cdot \left((\mathbf{u}^h \cdot \nabla_{\Gamma}^{\text{cov}}) \mathbf{u}^h - \mathbf{g}^h \right) - \text{div}_{\Gamma} \boldsymbol{\sigma}(\mathbf{u}^h, p^h) \right] = 0. \end{aligned}$$

The equations related to the different field equations were added up for brevity. The last row adds a stabilization term which is needed to obtain stable solutions for flows at high Reynolds numbers [12, 24]. In particular, the streamline upwind Petrov-Galerkin (SUPG) method is used for the stabilization. Different definitions of the stabilization parameter τ_{SUPG} are found [44, 49, 48] and

$$\tau_{\text{SUPG}} = \left[\left(\frac{2}{\Delta t} \right)^2 + \left(\frac{2 \|\mathbf{u}_e\|}{h_e} \right)^2 + \left(\frac{4\mu}{h_e^2} \right)^2 \right]^{-1/2}$$

is used herein with element-averaged velocity \mathbf{u}_e , element length h_e and $\Delta t \rightarrow \infty$ for the stationary case. When stabilization is not necessary because no oscillations occur, $\tau_{\text{SUPG}} = 0$. Note that in the stabilization term, second-order derivatives appear (only in the element interiors). The definition of *tangential* second-order derivatives is given, e.g., in [10].

Element assembly results in a *non*-linear system of equations of the form

$$\begin{bmatrix} \mathbf{K}^* + \mathbf{C}(\mathbf{u}) & \mathbf{G}^* & \mathbf{L} \\ \mathbf{G}^T & \mathbf{0} & \mathbf{0} \\ \mathbf{L}^T & \mathbf{0} & \mathbf{0} \end{bmatrix} \cdot \begin{bmatrix} \mathbf{u} \\ \mathbf{p} \\ \lambda \end{bmatrix} = \begin{bmatrix} \mathbf{f} \\ \mathbf{0} \\ \mathbf{0} \end{bmatrix}, \quad (3.33)$$

which is no longer symmetric (partly) due to the advection matrix $\mathbf{C}(\mathbf{u})$. The distinguishing feature of \mathbf{K}^* and \mathbf{G}^* (compared to \mathbf{K} and \mathbf{G} of the Stokes problem) are the added SUPG-stabilization terms. The issues related to mixed FEMs and the Babuška-Brezzi condition remain relevant.

3.3.5 Instationary Navier-Stokes flow

The discrete weak form of the instationary Navier-Stokes problem is: Given density $\varrho \in \mathbb{R}^+$, viscosity $\mu \in \mathbb{R}^+$, body force $\varrho \cdot \mathbf{g}^h(\mathbf{x}, t)$ in $\Gamma^h \times \tau$, traction $\hat{\mathbf{t}}^h(\mathbf{x}, t)$ on $\partial\Gamma_N^h \times \tau$, and initial condition $u_0^h(\mathbf{x})$ on Γ^h at $t = 0$ according to (3.11), find the velocity field $\mathbf{u}^h(\mathbf{x}, t) \in L_2(\tau; \mathcal{S}_u^h)$, pressure field $p^h(\mathbf{x}, t) \in L_2(\tau; \mathcal{S}_p^h)$, and Lagrange multiplier field $\lambda^h(\mathbf{x}, t) \in L_2(\tau; \mathcal{S}_\lambda^h)$ such that for all test functions $(\mathbf{w}_u^h, w_p^h, w_\lambda^h) \in \mathcal{V}_u^h \times \mathcal{V}_p^h \times \mathcal{V}_\lambda^h$, there

holds in $\Gamma^h \times \tau$

$$\begin{aligned} & \varrho \cdot \int_{\Gamma} \mathbf{w}_u^h \cdot \left(\partial_t \mathbf{u}^h + \left(\mathbf{u}^h \cdot \nabla_{\Gamma}^{\text{cov}} \right) \mathbf{u}^h - \mathbf{g}^h \right) dA + \int_{\Gamma} \nabla_{\Gamma}^{\text{dir}} \mathbf{w}_u^h : \boldsymbol{\sigma} \left(\mathbf{u}^h, p^h \right) dA + \int_{\Gamma} \boldsymbol{\lambda}^h \cdot \left(\mathbf{w}_u^h \cdot \mathbf{n}_{\Gamma}^h \right) dA \\ & - \int_{\partial\Gamma_N} \mathbf{w}_u^h \cdot \hat{\mathbf{t}}^h ds + \int_{\Gamma} w_p^h \cdot \text{div}_{\Gamma} \mathbf{u}^h dA + \int_{\Gamma} w_{\lambda}^h \cdot \left(\mathbf{u}^h \cdot \mathbf{n}_{\Gamma}^h \right) dA \\ & + \sum_{e=1}^{n_{\text{el}}} \int_{\Gamma_e} \tau_{\text{SUPG}} \left(\left(\mathbf{u}^h \cdot \nabla_{\Gamma}^{\text{cov}} \right) \mathbf{w}_u^h \right) \cdot \left[\varrho \cdot \left(\partial_t \mathbf{u}^h + \left(\mathbf{u}^h \cdot \nabla_{\Gamma}^{\text{cov}} \right) \mathbf{u}^h - \mathbf{g}^h \right) - \text{div}_{\Gamma} \boldsymbol{\sigma} \left(\mathbf{u}^h, p^h \right) \right] = 0. \end{aligned}$$

This yields a system of non-linear semi-discrete equations for $t \in \tau$

$$\begin{aligned} \mathbf{M} \cdot \dot{\mathbf{u}}(t) + (\mathbf{K}^* + \mathbf{C}(\mathbf{u})) \cdot \mathbf{u}(t) + \mathbf{G}^* \cdot \mathbf{p}(t) + \mathbf{L} \cdot \boldsymbol{\lambda}(t) &= \mathbf{f}(t), \\ \mathbf{G}^T \cdot \mathbf{u}(t) &= \mathbf{0}, \\ \mathbf{L}^T \cdot \mathbf{u}(t) &= \mathbf{0}, \end{aligned}$$

with initial condition $\mathbf{u}(0)$. This system may be advanced in time by using finite difference schemes and the Crank-Nicolson method is employed herein.

4 Numerical results

The following error measures are computed in the convergence studies. When analytic (exact) velocity and pressure fields, \mathbf{u}_{ex} and p_{ex} , are known, the velocity error is determined by

$$\varepsilon_{\mathbf{u}} = \sum_{i=1}^3 \sqrt{\int_{\Gamma} \left(u_i^h(\mathbf{x}) - u_{i,\text{ex}}(\mathbf{x}) \right)^2 dA} \quad (4.1)$$

and the pressure error calculated as

$$\varepsilon_p = \sqrt{\int_{\Gamma} \left(p^h(\mathbf{x}) - p_{\text{ex}}(\mathbf{x}) \right)^2 dA}. \quad (4.2)$$

When analytic solutions are not available, it is useful to evaluate the error of the FE approximations in the strong form of the momentum or continuity equations, integrated over the domain. For the example of stationary Stokes flow, the corresponding residual errors are defined as

$$\varepsilon_{\text{mom}} = \sqrt{\int_{\Gamma} \left(\mathbf{P} \cdot \text{div}_{\Gamma} \boldsymbol{\sigma} \left(\mathbf{u}^h, p^h \right) + \mathbf{f}^h \right)^2 dA} \quad (4.3)$$

and

$$\varepsilon_{\text{cont}} = \sqrt{\int_{\Gamma} (\text{div}_{\Gamma} \mathbf{u}^h)^2 \, dA}. \quad (4.4)$$

This can be easily extended to the case of Navier-Stokes flows where the advection term is added to the integrand in (4.3). Also the error in the tangential velocity constraint from Eq. (3.3) may be computed in a similar manner. The evaluation of the error ε_{mom} involves second-order derivatives and convergence can only be expected for higher-order elements and sufficiently smooth solutions.

4.1 Stokes flow on an axisymmetric surface

A test case is developed for which analytic solutions are available. An axisymmetric surface with height $L = 5$ and radius

$$r(z) = 1 + 1/5 \cdot \sin(1 + 3 \cdot z), \quad z \in [0, L],$$

is generated as illustrated in Fig. 2(a). Let $r_0 = r(0)$ and $r'_0 = \frac{dr(0)}{dz}$. In parametrized form, one may also define Γ based on the map $\mathbf{x}(\mathbf{a}) : \mathbb{R}^2 \rightarrow \mathbb{R}^3$,

$$\mathbf{x}(\mathbf{a}) = \begin{bmatrix} \cos a \cdot r(b) \\ \sin a \cdot r(b) \\ b \end{bmatrix} \quad \text{with } a \in [0, 2\pi], \quad b \in [0, 5].$$

The lower boundary at $z = 0$ is the Dirichlet boundary $\partial\Gamma_{\text{D}}$, where the inflow in co-normal direction of the manifold is prescribed as

$$\hat{\mathbf{u}}(\mathbf{x}) = \frac{\mathbf{u}^*}{\|\mathbf{u}^*\|} \quad \text{and} \quad \mathbf{u}^* = \begin{bmatrix} r'_0 \cdot \cos \theta \\ r'_0 \cdot \sin \theta \\ 1 \end{bmatrix},$$

with angle θ given by $\tan \theta = y/x$. The upper boundary at $z = L$ is the outflow boundary where zero-tractions are applied as Neumann boundary conditions. The density and viscosity are set to $\varrho = 1$ and $\mu = 0.01$, respectively.

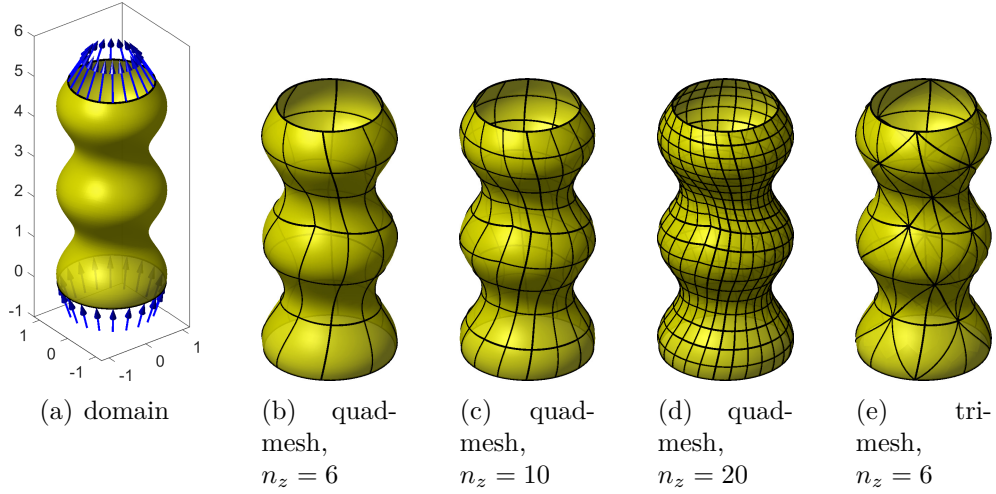


Figure 2: Manifold for the axisymmetric test case and meshes with different resolutions. In (a), the blue arrows indicate the direction of the flow at the inflow (bottom) and outflow (top) boundaries.

The mass flow on the lower boundary is

$$Q_0 = \int_{\partial\Gamma_D} \hat{\mathbf{u}}(\mathbf{x}) \cdot \mathbf{n}_{\partial\Gamma} ds = 2\pi \cdot r_0$$

and due to mass conservation, the mass flow along the height follows as $Q(z) = 2\pi \cdot r_0/r(z)$. As the flow field is expected to be axisymmetric for this test case, and the tangential velocity constraint applies, one may compute the velocity components as

$$\begin{bmatrix} u_{\text{ex}}(\mathbf{x}) \\ v_{\text{ex}}(\mathbf{x}) \\ w_{\text{ex}}(\mathbf{x}) \end{bmatrix} = \frac{r_0}{r \cdot \sqrt{1 + \left(\frac{dr}{dz}\right)^2}} \cdot \begin{bmatrix} \frac{dr}{dz} \cdot x/r \\ \frac{dr}{dz} \cdot y/r \\ 1 \end{bmatrix}.$$

See Fig. 3 for a graphical representation. It is noted that the mass flow $Q(z)$, velocity magnitude $\|\mathbf{u}\|$, and the vertical velocity component w are only functions of z , that is, they do not vary in x - and y -directions.

Finite element approximations are carried out on various meshes composed by triangular or quadrilateral Lagrange elements of different orders. For the convergence studies, meshes with $n_z = \{4, 6, 10, 14, 20, 30, 40, 60\}$ elements over the height are chosen; the number of elements in circumferential direction is $n_\theta = \text{round}(2\pi r_0/L \cdot n_z)$. The meshes are perturbed, as illustrated in Figs. 2(b) to (d), to avoid perfectly axisymmetric meshes which, otherwise,

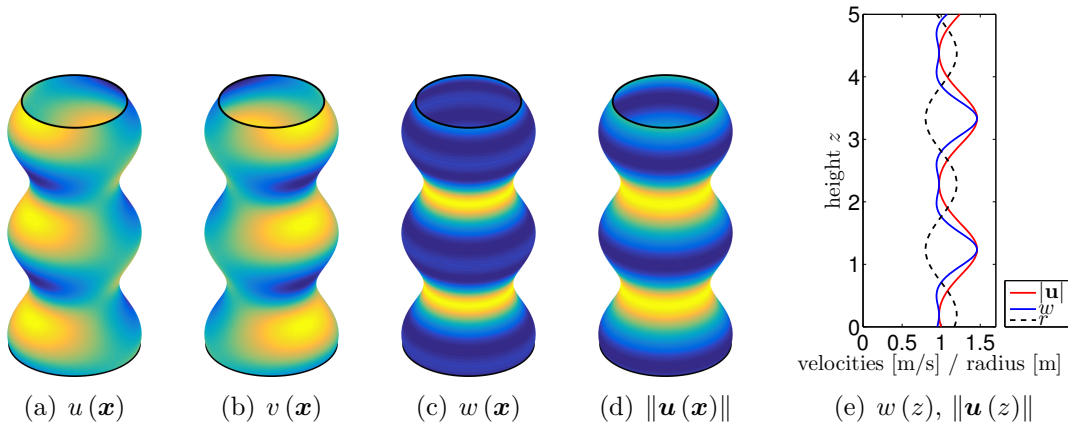


Figure 3: Exact solution for the axisymmetric test case.

could have improved the convergence rates for this special case.

The individual element orders used for the convergence studies are indicated by a 4-tuple $\{k_{\text{geom}}, k_{\mathbf{u}}, k_p, k_\lambda\}$. To be precise, this tuple summarizes the employed orders for the geometry, k_{geom} , the velocities, $k_{\mathbf{u}}$, the pressure, k_p , and the Lagrange multiplier for enforcing the tangential velocity constraint, k_λ . For each tuple, meshes with different resolutions (given by n_z and n_θ) are considered and errors calculated, each time resulting in one curve in the convergence plots as indicated in the legends.

Systematic studies of different combinations of element orders showed that equal-order approximations for the velocity and pressure, i.e., $k_p = k_{\mathbf{u}}$ do not converge satisfactory (or at all), which is well-known from the standard context of the incompressible Navier-Stokes equations in 2D and 3D due to the Babuška-Brezzi condition. For the studies outlined in this paper, we shall choose $k_p = k_{\mathbf{u}} - 1$ which is a popular choice for FEM approximations of classical incompressible flows and known as Taylor-Hood elements [46].

For the first study, we use $2 \leq k_{\mathbf{u}} \leq 5$, $k_p = k_{\mathbf{u}} - 1$, and $k_\lambda = k_{\mathbf{u}} - 1$ which, later on, becomes the recommended standard setting. Convergence plots for $\varepsilon_{\mathbf{u}}$ and ε_p are given in Fig. 4. The thick solid lines are for $k_{\text{geom}} = k_{\mathbf{u}} + 1$. It is noteworthy that for quadrilateral elements, setting $k_{\text{geom}} = k_{\mathbf{u}}$ leads to almost identical results as seen from the thin dashed lines in Figs. 4(c) and (d). This does not necessarily hold for triangular elements, see Figs. 4(a) and (b), where the convergence may drop by one order when setting $k_{\text{geom}} = k_{\mathbf{u}}$ rather than $k_{\text{geom}} = k_{\mathbf{u}} + 1$. This is later confirmed for the errors ε_{mom} and $\varepsilon_{\text{cont}}$ in Fig. 6. Therefore, we recommend to choose the geometry one order higher than $k_{\mathbf{u}}$ which is done in the remainder of this work. Another reason is that the normal vector \mathbf{n} is present in

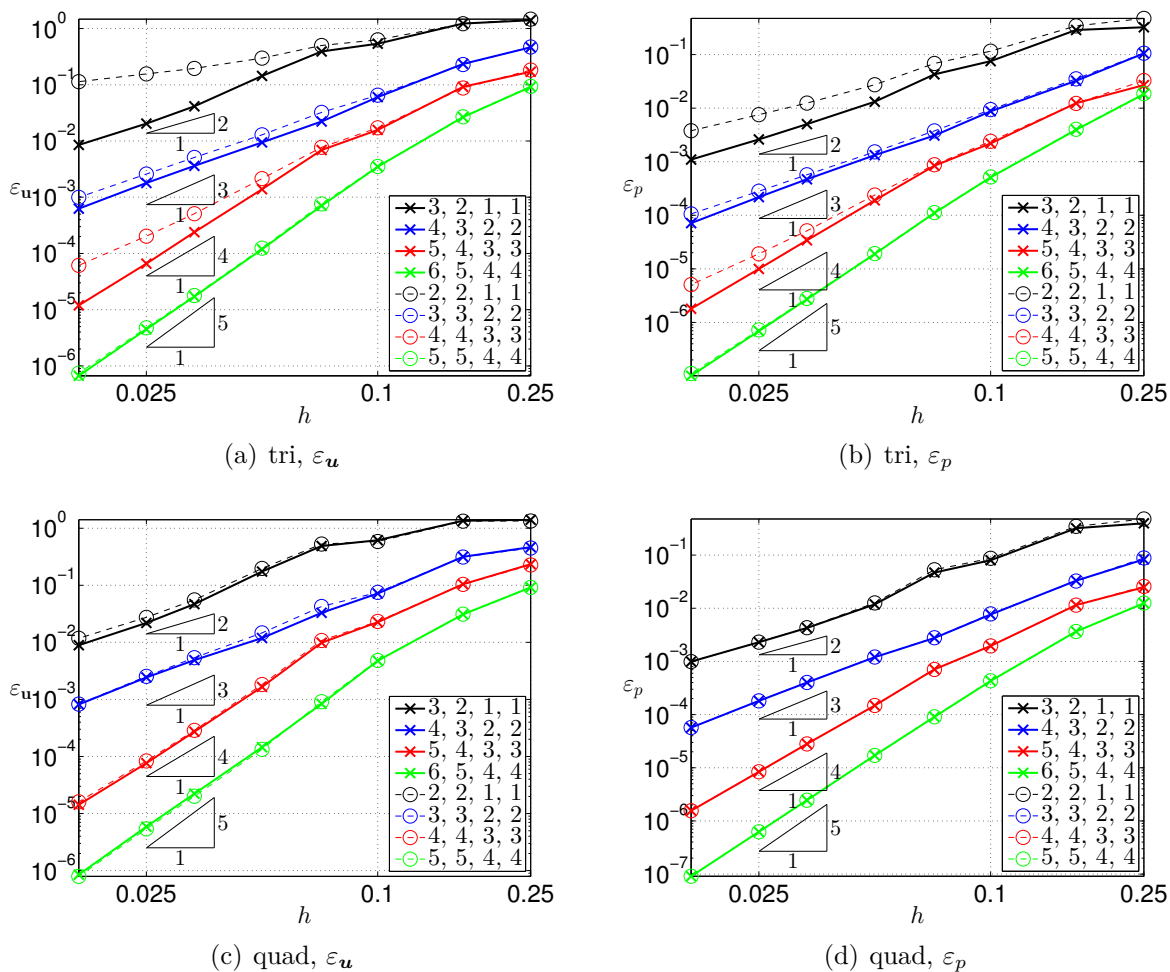


Figure 4: Convergence results in ε_u and ε_p for the axisymmetric test case, (a) and (b) for triangular elements, (c) and (d) for quadrilateral elements. The legends decode the orders $\{k_{\text{geom}}, k_u, k_p, k_\lambda\}$ of the meshes.

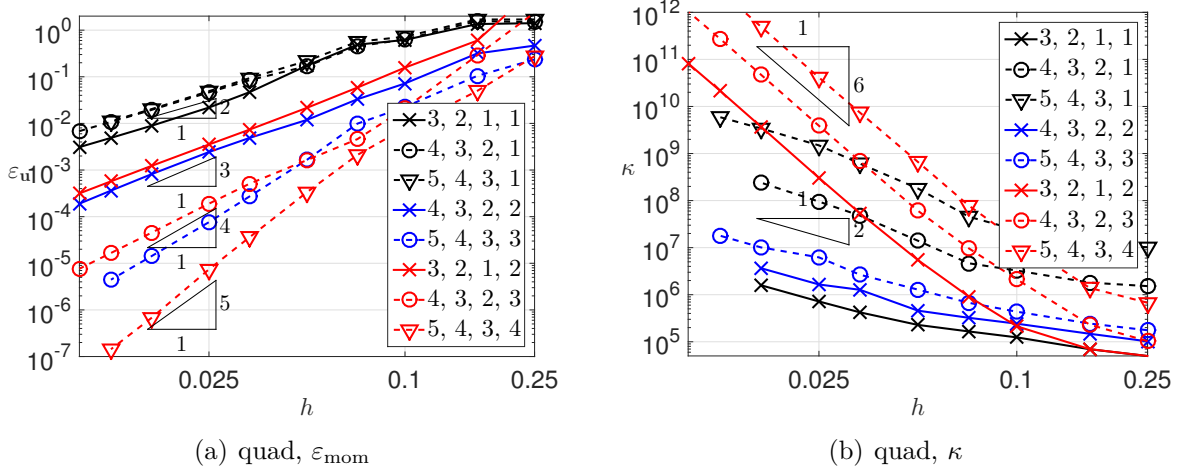


Figure 5: Influence of the order of the Lagrange multiplier field for enforcing the tangential velocity constraint: (a) convergence results in $\varepsilon_{\mathbf{u}}$ and (b) conditioning κ for the axisymmetric test case.

the governing equations and is computed based on the Jacobi matrix, i.e., first derivatives of the element mappings of order k_{geom} are involved.

It is important to note in Fig. 4 that the convergence rates in the pressure are optimal, $m_p = k_p + 1$, however, in the velocities one order sub-optimal, $m_{\mathbf{u}} = k_{\mathbf{u}}$. We have traced this back to the influence of the order k_λ of the Lagrange multiplier field. This is demonstrated in Fig. 5 where (a) shows the error $\varepsilon_{\mathbf{u}}$ and (b) the condition number κ of the corresponding system of equations (obtained with Matlab's `cond`-function). As before, $k_{\text{geom}} = k_{\mathbf{u}} + 1$ and $k_p = k_{\mathbf{u}} - 1$. Fig. 4 shows that setting $k_\lambda = 1$ yields convergence rates $m_{\mathbf{u}} = 2$ independent of the other orders (black lines). Setting $k_\lambda = k_{\mathbf{u}}$ yields *optimal* convergence rates $m_{\mathbf{u}} = k_{\mathbf{u}} + 1$ for the velocities (red lines), however, there is a dramatic influence on the conditioning which scales with $\kappa \sim O(h^{-6})$ in this case rather than with $O(h^{-2})$ for all choices where $k_\lambda < k_{\mathbf{u}}$. Therefore, we set $k_\lambda = k_{\mathbf{u}} - 1$ in the following and accept the sub-optimal convergence in the velocities.

Next, the error is observed in the strong form of the momentum and continuity equations, ε_{mom} and $\varepsilon_{\text{cont}}$, see Eqs. (4.3) and (4.4). Results for $k_p = k_\lambda = k_{\mathbf{u}} - 1$ are depicted in Fig. 6 for triangular and quadrilateral elements. Again, the thick lines refer to $k_{\text{geom}} = k_{\mathbf{u}} + 1$ and the thin dashed lines to $k_{\text{geom}} = k_{\mathbf{u}}$. As mentioned above for the L_2 -errors in the velocities and pressure, this makes a difference (of one order) for triangular elements, however, not for quadrilateral elements. When using $k_{\text{geom}} = k_{\mathbf{u}} + 1$ on the safe side, the convergence

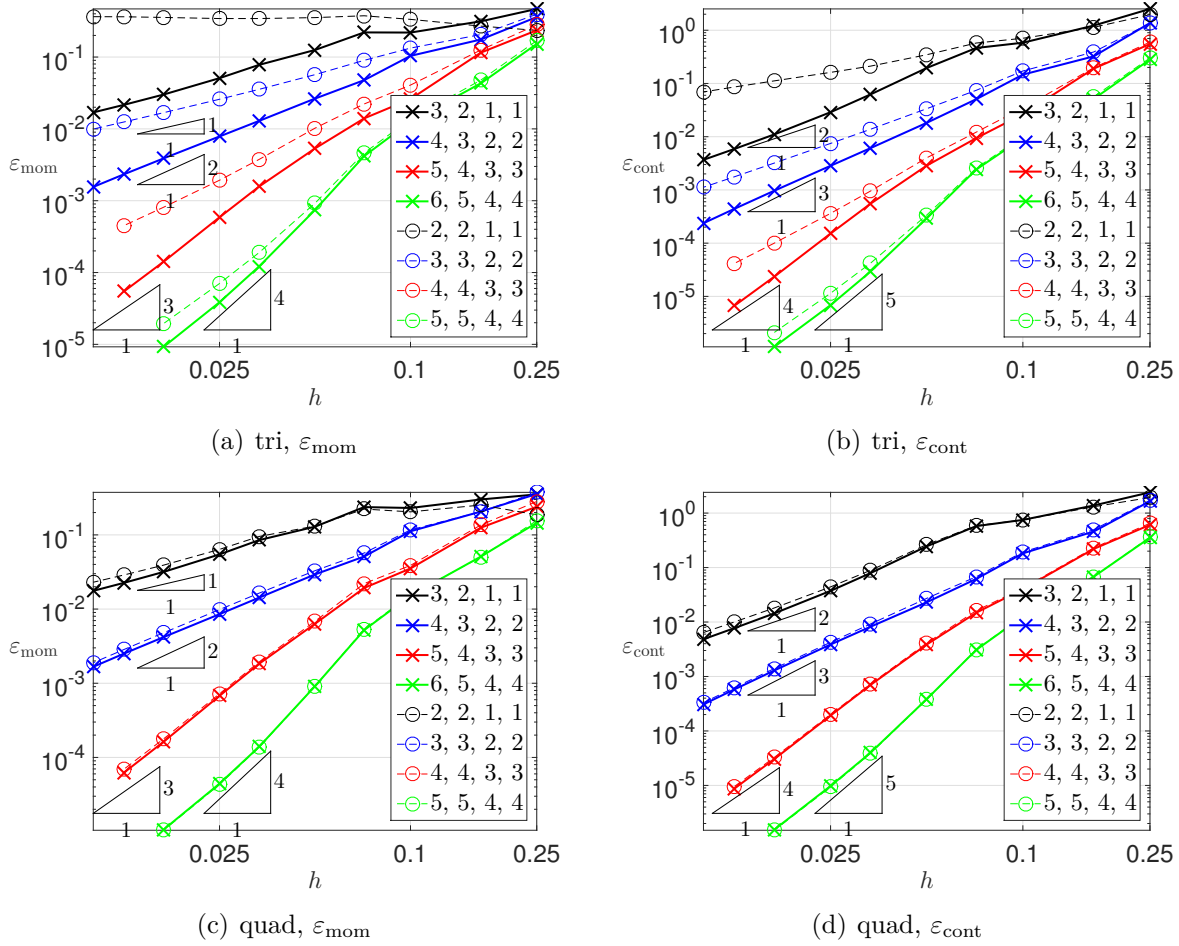


Figure 6: Convergence results in ε_{mom} and $\varepsilon_{\text{cont}}$ for the axisymmetric test case, (a) and (b) for triangular elements, (c) and (d) for quadrilateral elements. The legends decode the orders $\{k_{\text{geom}}, k_{\mathbf{u}}, k_p, k_\lambda\}$ of the meshes.

rate in ε_{mom} is $m_{\text{mom}} = k_{\mathbf{u}} - 1$ as expected due to the presence of second-order derivatives of \mathbf{u} in the momentum equations. The expected convergence rate in $\varepsilon_{\text{cont}}$ is $m_{\text{cont}} = k_{\mathbf{u}}$ due to the presence of first order derivatives of \mathbf{u} in the continuity equation.

4.2 Driven cavity flows on manifolds

The stationary Navier-Stokes model is considered in this example. Starting point is the driven cavity for the case of a flat 2D domain as depicted in Fig. 7(a). This case has well-documented reference solutions for a variety of Reynolds numbers [21]. There, a flow inside a quadratic domain $\Omega_{2\text{D}} = (0, 1) \times (0, 1)$ with no-slip boundary conditions on the

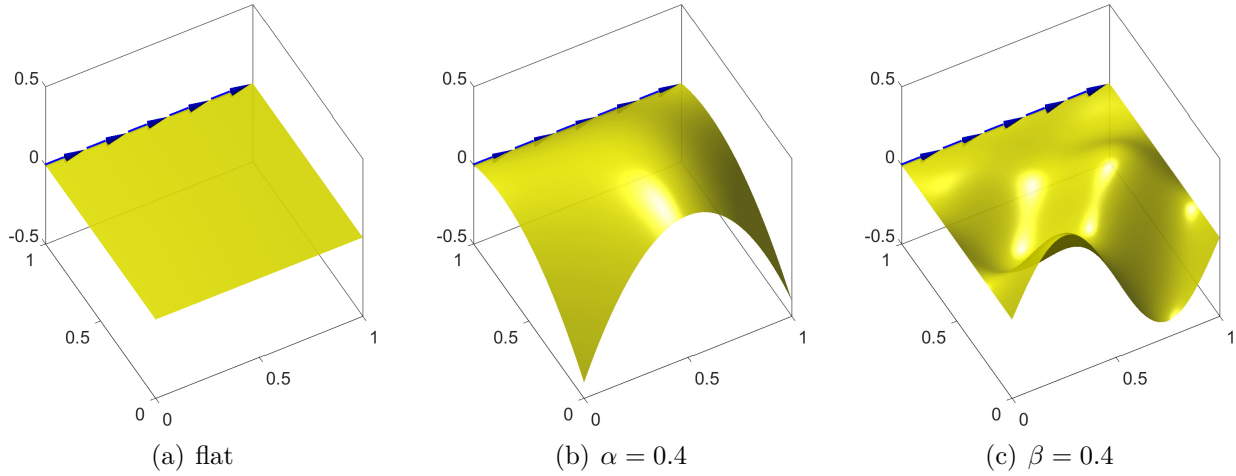


Figure 7: Different manifolds for the driven cavity test case, (a) flat, (b) map A with $\alpha = 0.4$, and (c) map B with $\beta = 0.4$.

left, right and lower wall develops under a shear flow of $u = 1.0$ and $v = 0.0$ applied on the upper boundary until a stationary solution is reached. The Reynolds number is computed as $Re = \varrho \cdot u \cdot L / \mu$.

Herein, the situation is extended to curved surfaces in 3D by deforming the flat 2D domain Ω_{2D} in z -direction using functions $z(x, y)$. In particular, two different maps A and B are used,

$$\begin{aligned} \text{map A : } \quad z(x, y) &= \alpha \cdot (-1 + 8x + 2y - 8x^2) \cdot (1 - y), \\ \text{map B : } \quad z(x, y) &= \beta \cdot (1 - y) \cdot \sin((2x - 1)\pi) \cdot \cos((2y - 1)\pi), \end{aligned}$$

where α and β scale the height in z -direction, see Figs. 7(b) and (c) for examples. The advantage is that for $\alpha = 0$ and $\beta = 0$, the flat situation is recovered and the reference solutions in [21] are relevant. We have confirmed that these solutions are recovered with great accuracy also for any rigid body transformation of Ω_{2D} into three dimensions. The density is chosen as $\varrho = 1$ and two different viscosities of $\mu = 0.01$ and $\mu = 0.001$ leading to Reynolds numbers of $Re = 100$ and $Re = 1000$ for the flat case, respectively. Solutions for the velocity magnitude and pressure field for some example manifolds are displayed in Fig. 8.

The meshes feature quadrilateral elements of different orders and are refined towards the boundaries to capture the resulting boundary layers. See Fig. 9 for the meshes in Ω_{2D} which

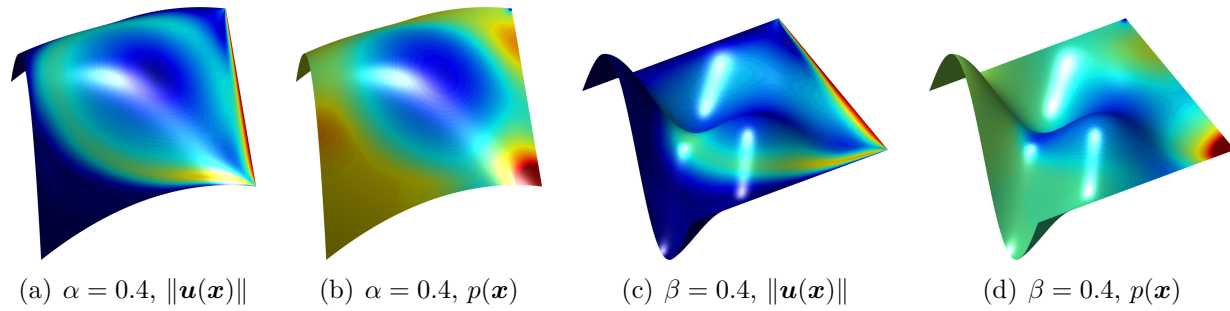


Figure 8: Velocity and pressure fields for the driven cavity test case with $\mu = 0.001$ for map A with $\alpha = 0.4$ and map B with $\beta = 0.4$.

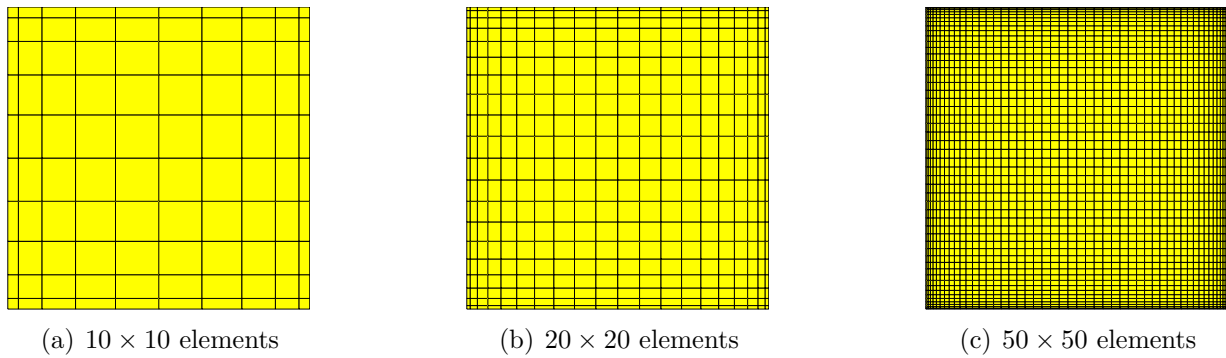


Figure 9: Different meshes for the driven cavity test case in top view.

are mapped to 3D according to map A and B from above for various scaling coefficients α and β . The number of elements per dimension is $n = \{10, 20, 30, 50, 70, 100\}$. For the numerical studies, $k_p = k_\lambda = k_u - 1$ and $k_{\text{geom}} = k_u + 1$ is used as recommended above.

Just as for the reference solutions in [21], the results are presented as velocity profiles along the horizontal and vertical centerlines in Ω_{2D} . Fig. 10 shows the profiles for the velocity component u along the vertical centerline and v along the horizontal centerline for the two maps with different scaling factors α and β , respectively. The crosses indicating the reference solution from [21] are only relevant for the flat case where $\alpha = \beta = 0$. The results for the velocity component w along the two centerlines are given in Fig. 11. These results have the quality of benchmark solutions and have been obtained with $k_u = 4$ and 100 elements per dimensions. The convergence of other element orders and mesh resolutions towards these profiles has been confirmed, and a small selection is shown in Fig. 12. Without stabilization, the typical oscillations are seen for this rather high Reynolds number for coarse meshes with low order. As no analytical solutions for the velocities and pressure are available, it is impossible to provide convergence results in ε_u and ε_p . Furthermore, the singular pressure in the upper left and right corners lead to singularities in the derivatives of other physical fields. Thus, it cannot be expected that (optimal) convergence in ε_{mom} and $\varepsilon_{\text{cont}}$ is achieved.

4.3 Flows on zero-level sets

The next test case shows the potential to solve flows on zero-level sets with the proposed models. Stationary Stokes and Navier-Stokes flows are considered. The scalar function $\phi(\mathbf{x}) : \mathbb{R}^3 \rightarrow \mathbb{R}$ is based on [14] and defined as

$$\begin{aligned} \phi(\mathbf{x}) = & (x^2 + y^2 - 4)^2 + (x^2 + z^2 - 4)^2 + (y^2 + z^2 - 4)^2 + \\ & (x^2 - 1)^2 + (y^2 - 1)^2 + (z^2 - 1)^2 - 15. \end{aligned}$$

The zero-isosurface of ϕ implies the compact manifold of interest, $\Gamma = \{\mathbf{x} : \phi(\mathbf{x}) = 0\}$ and is depicted in Fig. 13. In a first step, meshes with linear triangular elements are generated using `distmesh` [39]. A scaling parameter h may be chosen which defines an average element length. In a second step, higher-order elements are mapped to this linear surface mesh and their element nodes are “lifted” [14] such that they are on the manifold Γ . Thereby, a higher-order accurate representation Γ^h is obtained.

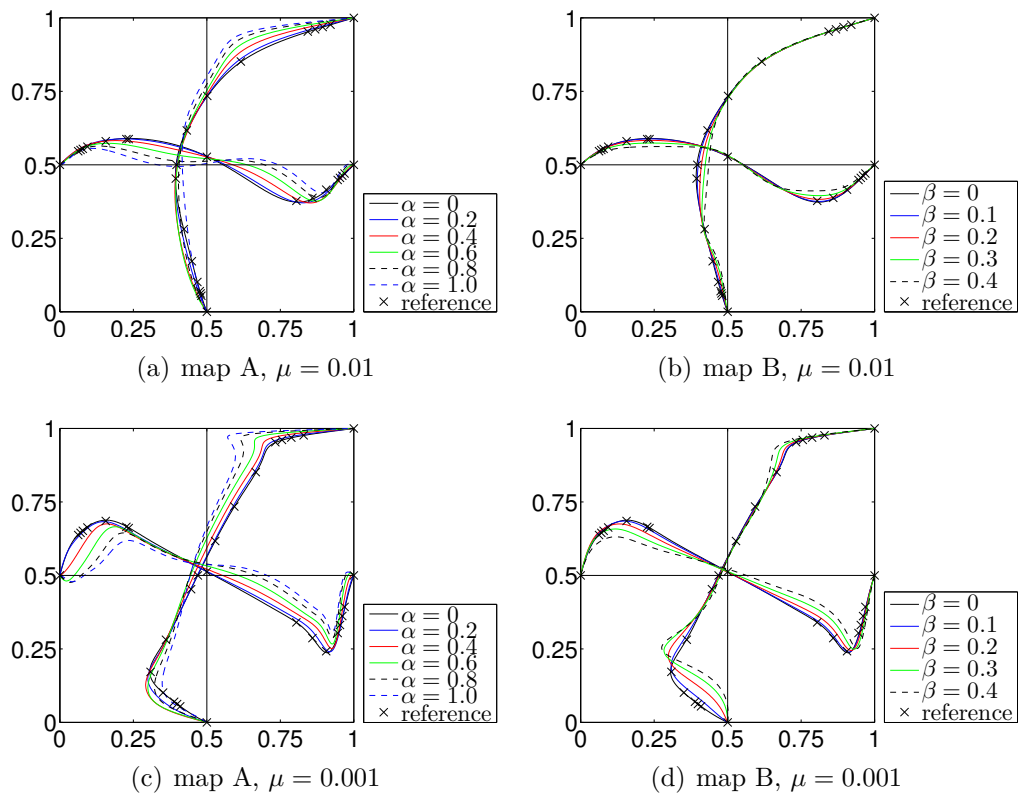


Figure 10: Velocity profiles for the driven cavity test case for different α and β . The vertical profiles show the velocity component $u(\mathbf{x})$, the horizontal profiles $v(\mathbf{x})$. The scaling factor of the velocities is 0.5.

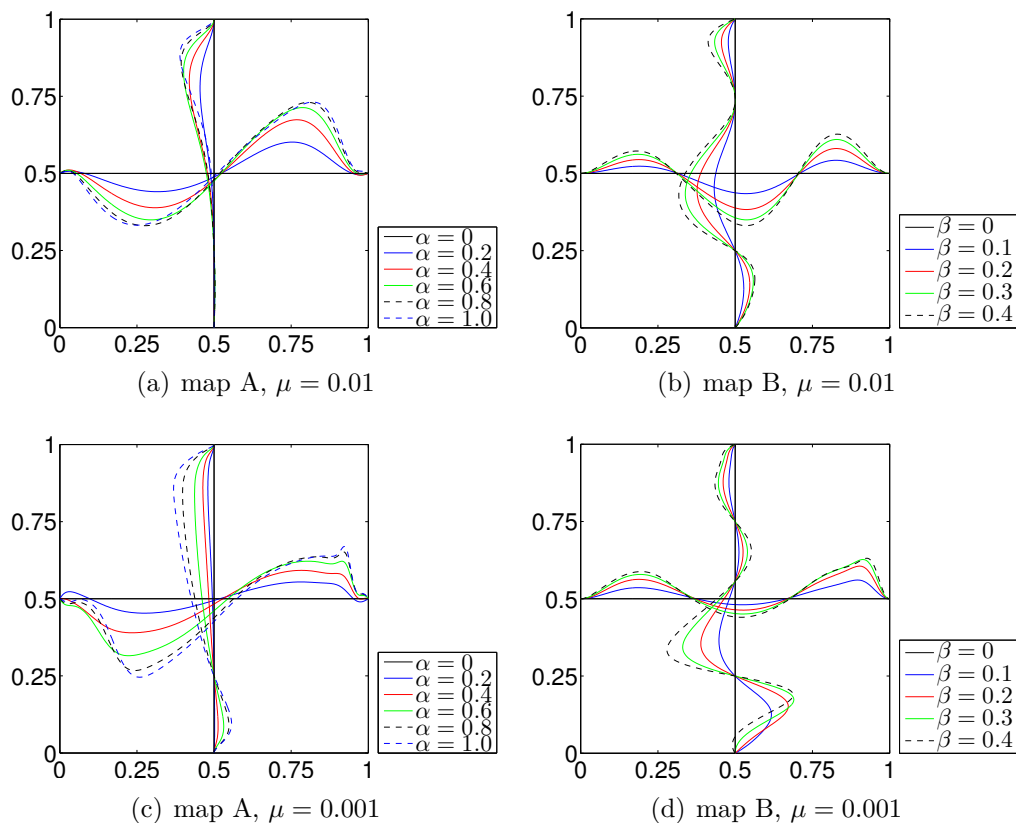


Figure 11: Velocity profiles for the driven cavity test case for different α and β . The horizontal and vertical profiles show the velocity component $w(\mathbf{x})$ scaled by the factor 1.

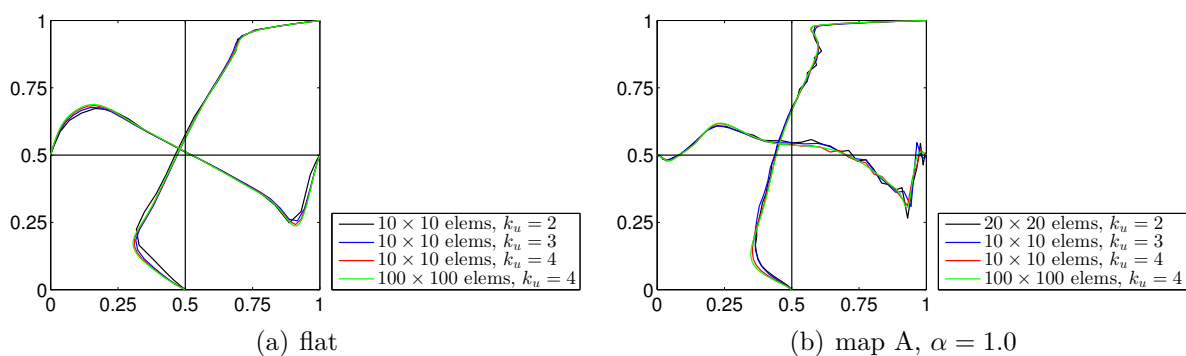


Figure 12: Velocity profiles for the driven cavity test case following Fig. 10. Results of coarse meshes with 10×10 elements are compared to the high-accuracy results from above (with 100×100 elements with $k_u = 4$), (a) flat manifold, (b) manifold according to map A with $\alpha = 1.0$.

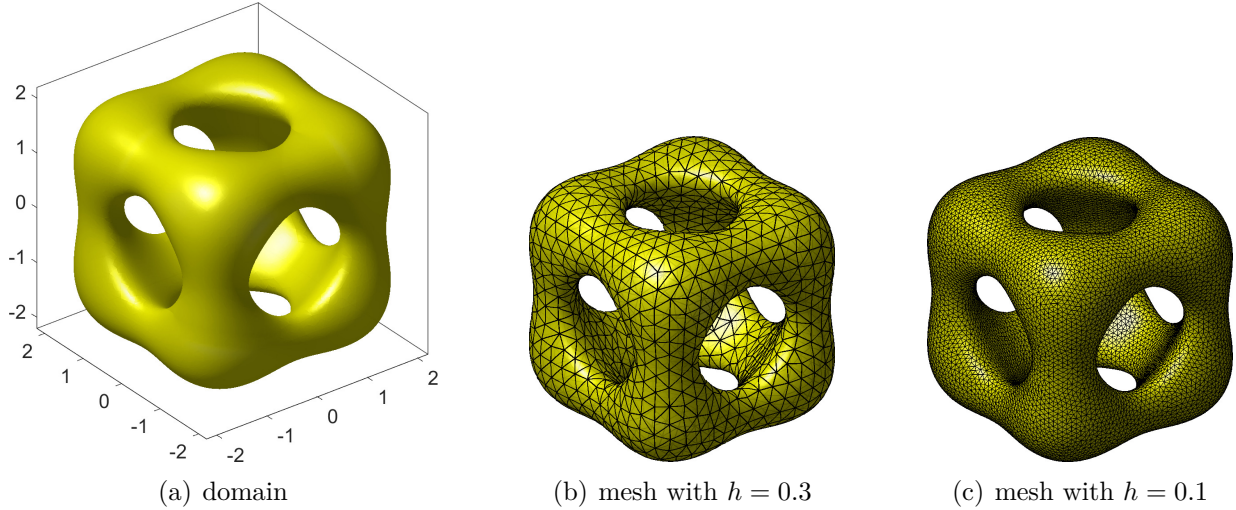


Figure 13: Manifold for the zero-isosurface test case and meshes with different resolutions.

As there are no boundaries present, an acceleration field in z -direction drives the flow. That is, on the right hand side, $\mathbf{g} = \mathbf{P} \cdot [0, 0, g_z]^\top$ where g_z is determined by

$$g_z(\mathbf{x}) = \begin{cases} \exp\left(-\frac{z^2}{2\sigma_0^2}\right) & \text{with } \sigma_0 = 0.15 \text{ for } x < 0 \text{ and } y < 0, \\ 0 & \text{else,} \end{cases}$$

and visualized in Fig. 14(a). It is virtually non-zero only for the left front “pillar” of the domain. The density is $\varrho = 1$ and the viscosity is $\mu = 0.05$. For the case of stationary Navier-Stokes flow, the corresponding velocity magnitude, pressure fields and vorticity ω^* according to Eq. (3.8) are seen in Figs. 14(b) to (d), respectively.

In the numerical studies, $2 \leq k_u \leq 5$, $k_p = k_\lambda = k_u - 1$, and $k_{\text{geom}} = k_u + 1$ are used. As there is no analytical solution available, convergence results are only shown in ε_{mom} and $\varepsilon_{\text{cont}}$ in Fig. 15. Higher-order rates are clearly achieved. In order to make the solution more quantitative, the velocity profiles for $w(\mathbf{x})$ in the horizontal xy -plane (at $z = 0$) are shown in Fig. 16. The four closed black lines represent the intersection of the plane with the vertical “pillars” of the zero-isosurface. Fig. 16(a) shows $w(\mathbf{x})$ as a third dimension, and (b) shows the same result where $w(\mathbf{x})$ is plotted in normal direction of the plane-pillar intersections with a scaling factor of 0.4. A clear convergence to these profiles was observed when using meshes with different resolutions and orders.

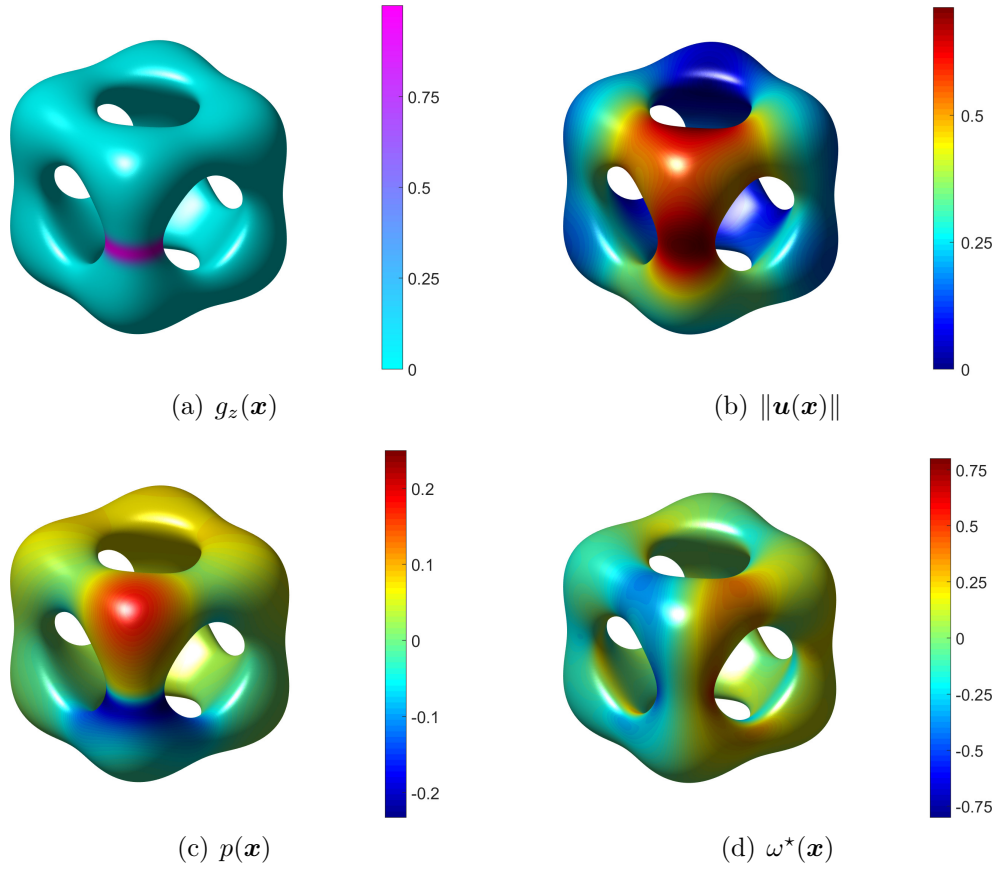


Figure 14: Physical fields of the zero-isosurface test case: (a) acceleration g_z , (b) velocity magnitude $\|\mathbf{u}\|$, (c) pressure p , (d) vorticity ω^* .

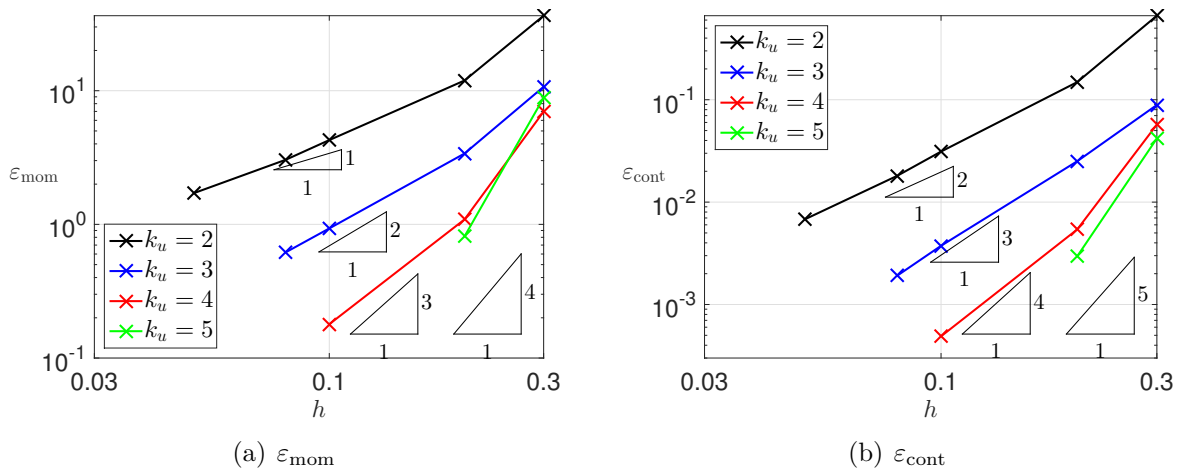


Figure 15: Convergence results in (a) ε_{mom} and (b) $\varepsilon_{\text{cont}}$ for the zero-isosurface test case.

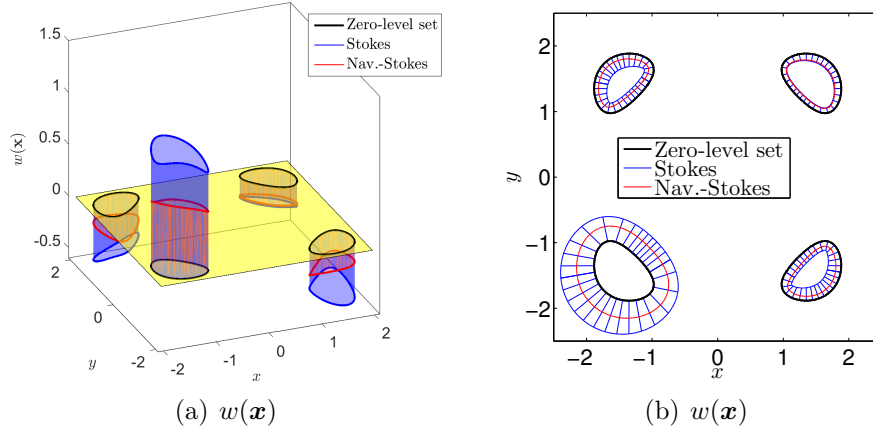


Figure 16: Profiles for the vertical velocity $w(\mathbf{x})$ in the plane with $z = 0$, the scaling factor in (b) is 0.4.

4.4 Cylinder flows

As an example for the instationary Navier-Stokes equations, the following test case is based on a channel flow around a cylinder according to [42]. The geometry is first described in 2D, labelled Ω_{2D} , and later on mapped to obtain curved surfaces in 3D. In 2D, the cylinder with a diameter of 0.1 is placed slightly unsymmetrically in y -direction of the channel in $[0, 2.20] \times [0, 0.41]$, see Fig. 17(a). No-slip boundary conditions are applied on the upper and lower wall and on the cylinder surface. A quadratic velocity profile for u , with $u_{\max} = 1.5$, and $v = 0$ is applied at the inflow on the left side of the domain. At the outflow, traction-free boundary conditions are used. The density and viscosity are prescribed as $\rho = 1.0$ and $\mu = 0.001$. This results in a Reynolds number of $\text{Re} = \rho \cdot u_m \cdot L / \mu = 100$ when taking the cylinder diameter as a length scale L and the average inflow velocity $u_m = 1.0$ at the inflow. At this Reynolds number, periodic flow patterns known as the Kármán vortex street are observed behind the cylinder. Reference solutions are given for the lift and drag coefficients c_L and c_D of the cylinder [42] and the current implementation confirms these numbers for the flat case (i.e., in 2D or when the flat 2D domain is transformed by a rigid body motion to 3D). The reference Strouhal number $\text{St} = D / (u_m T)$, with the diameter $D = 0.1$ of the cylinder, and the time T for 2 periods of the curve of c_D , is given as $0.295 \leq \text{St} \leq 0.305$, resulting in a frequency of about $f = 3.33 \text{ 1/s}$.

The 2D domain is mapped to three dimensions using two different maps. Assume that the coordinates of the 2D domain Ω_{2D} , as seen in Fig. 17(a), are given in coordinates (a, b) .

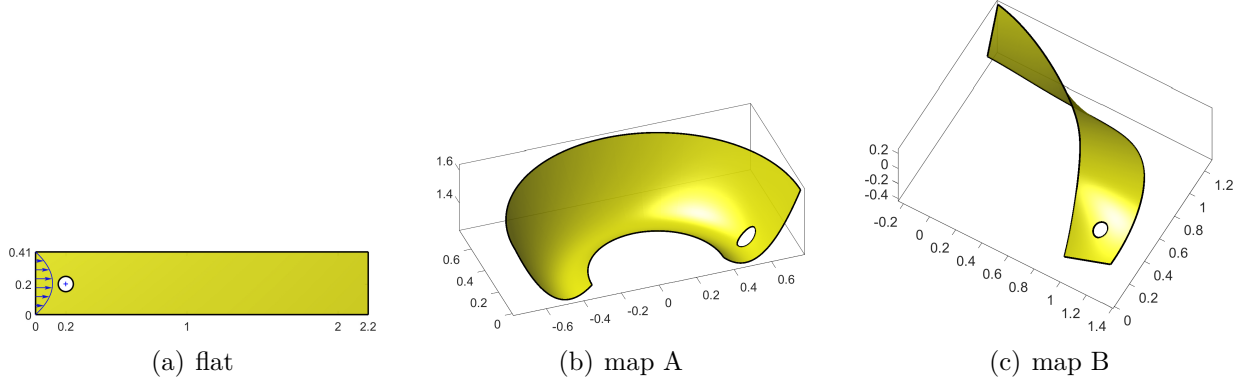


Figure 17: Manifolds for the cylinder flow test case.

Map A, $\mathbf{x}(\mathbf{a}) : \mathbb{R}^2 \rightarrow \mathbb{R}^3$, is defined as

$$\begin{aligned} x(\mathbf{a}) &= \cos\left(\frac{\pi \cdot a}{2.2}\right) \cdot (b + 0.35), \\ y(\mathbf{a}) &= \sin\left(\frac{\pi \cdot a}{2.2}\right) \cdot (b + 0.35), \\ z(x(\mathbf{a}), y(\mathbf{a})) &= 2 + 1/2\sqrt{x^2 + y^2} - \sin\left(3\sqrt{x^2 + y^2}\right). \end{aligned}$$

For map B, we first define an intermediate mapping $\mathbf{r}(\mathbf{a}) : \mathbb{R}^2 \rightarrow \mathbb{R}^3$ applying some twist to the domain,

$$\begin{aligned} r(\mathbf{a}) &= a, \\ s(\mathbf{a}) &= -(1 + q(a)) \cdot (b - 0.205) \cdot \cos(\pi/6(1 - 25/11 \cdot a)), \\ t(\mathbf{a}) &= -(1 + q(a)) \cdot (b - 0.205) \cdot \sin(\pi/6(1 - 25/11 \cdot a)). \end{aligned}$$

with $q(a) = -0.2/2.42 \cdot a^2 + 0.44/2.42 \cdot a$. This is further mapped by $\mathbf{x}(\mathbf{r}) : \mathbb{R}^3 \rightarrow \mathbb{R}^3$ defined as

$$\begin{aligned} x(\mathbf{r}) &= \cos(50/198 \cdot \pi \cdot r) \cdot (s + 6/5), \\ y(\mathbf{r}) &= \sin(50/198 \cdot \pi \cdot r) \cdot (s + 6/5), \\ z(\mathbf{r}) &= t + 1/5 \sin(3r). \end{aligned}$$

The resulting curved manifolds according to map A and B are visualized in Figs. 17(b) and (c), respectively. Note that also the inflow velocities are mapped accordingly based on the Jacobians of the respective mappings to ensure that they are in the tangent space at

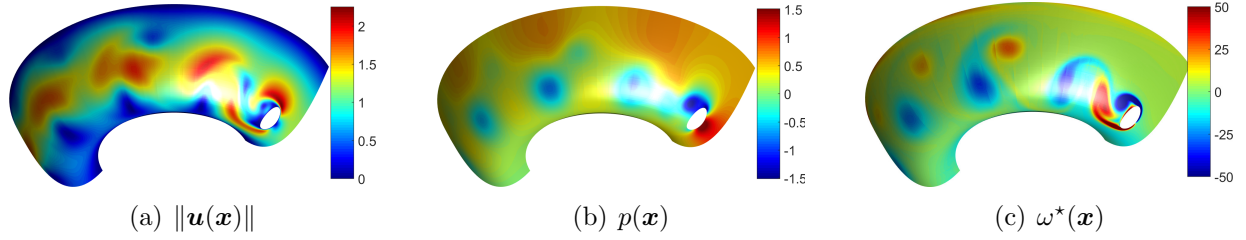


Figure 18: Physical fields for the cylinder flow test case according to map A: (a) velocity magnitude $\|\mathbf{u}\|$, (b) pressure p , (c) vorticity ω^* .

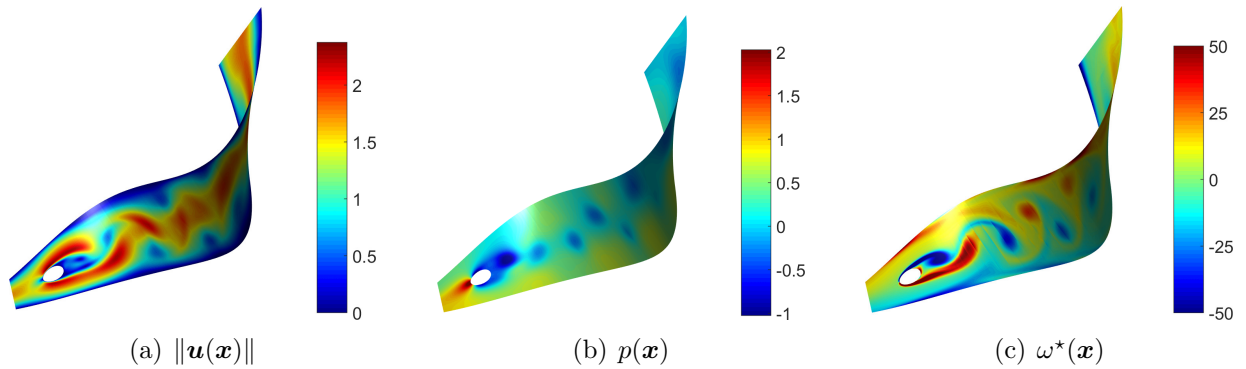


Figure 19: Physical fields for the cylinder flow test case according to map B: (a) velocity magnitude $\|\mathbf{u}\|$, (b) pressure p , (c) vorticity ω^* .

$\partial\Gamma_D$.

The initial condition on the manifolds is $\mathbf{u}_0(\mathbf{x}) = \mathbf{0}$. The observed time interval is $\tau = [0, 6]$ and the inflow velocities are ramped by a cubic function in time,

$$R(t) = \begin{cases} -2 \cdot (t/t^*)^3 + 3 \cdot (t/t^*)^2 & \text{for } t \leq t^*, \\ 1 & \text{else,} \end{cases}$$

with $t^* = 0.96$. That is, after t^* , the full velocity profile is active at the inflow. Figs. 18 and 19 show the velocity magnitude, pressure field, and vorticity ω^* at time $t = 6$ for the two mappings. The expected vortex shedding can be clearly seen.

Two different meshes with 972 and 1920 elements each are used which are refined at the no-slip boundaries to resolve the boundary layers. They are visualized for Ω_{2D} in Fig. 20 and mapped to the manifolds accordingly. We use element orders of $k_{\text{geom}} = 4$, $k_u = 3$, $k_p = 2$ and $k_\lambda = 2$ in the numerical studies shown here. Higher orders achieved virtually indistinguishable results for the quantities shown below. It is also noted that the

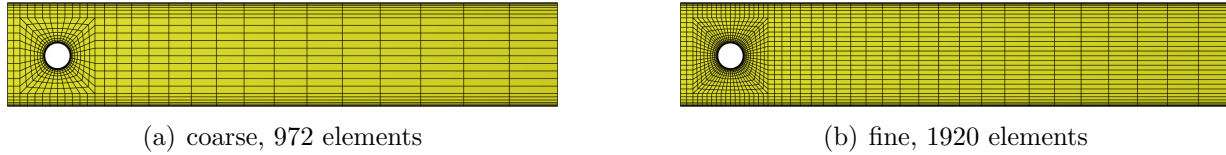


Figure 20: Coarse and fine mesh for the cylinder flow test case; these meshes are later mapped according to map A or B.

Crank Nicolson method used for the time discretization is only second-order accurate. For the time discretization $n_{\text{step}} = \{150, 300, 600, 1200, 2400, 4800\}$ time steps are used. To make the results more quantitative, the stresses at the cylinder wall are summed up to obtain a force resultant $F(t) = \|\mathbf{F}(t)\|$ in 3D. This is the equivalent of the lift and drag coefficients for the flat 2D case. Furthermore, the pressure difference between the front and back position of the cylinder (in Ω_{2D} , mapped to three dimensions) is computed, i.e., $\Delta p(t) = p_{\text{front}}(t) - p_{\text{back}}(t)$.

The results for map A are shown in Fig. 21 for the different number of time steps. It can be seen that after about 2s, the expected vortex shedding is almost established. After 3s, the resulting oscillations remain virtually unchanged. The time interval [5.2, 6] is shown in more detail in Figs. 21(b) and (d) for $F(t)$ and $\Delta p(t)$, respectively. The convergence with increasing number of time steps is clearly demonstrated. Fig. 22 shows the results in the same style for map B; the same conclusions may be drawn. The spatial convergence is investigated in Fig. 23 where it is found that the coarse and fine mesh employed here obtain very similar results for the chosen element orders. The frequency of the oscillations for map A is $f_A = 2.191 \text{ 1/s}$ and for map B is $f_B = 3.078 \text{ 1/s}$; for the flat case the frequency is $f = 3.33 \text{ 1/s}$.

5 Conclusions

The surface FEM with higher-order elements is applied to solve Stokes and Navier-Stokes flows on (fixed) manifolds. For the governing equations, the classical gradient and divergence operators are replaced by their tangential counterparts. An additional constraint is needed to ensure that the velocities are in the tangent space of the manifold. Stabilization is required for the case of Navier-Stokes flows at large Reynolds numbers and the standard streamline-upwind Petrov-Galerkin (SUPG) approach is used herein.

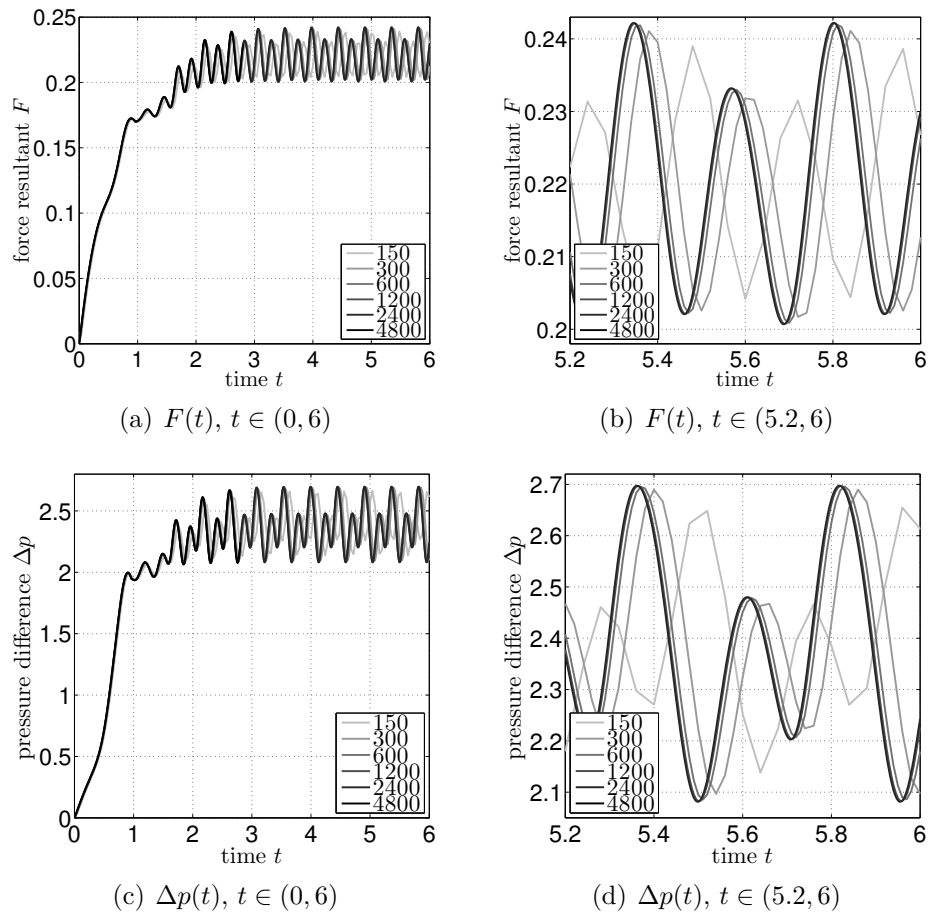


Figure 21: Force resultant $F(t)$ and pressure difference $\Delta p(t)$ obtained on the fine mesh of the cylinder flow test case according to map A.

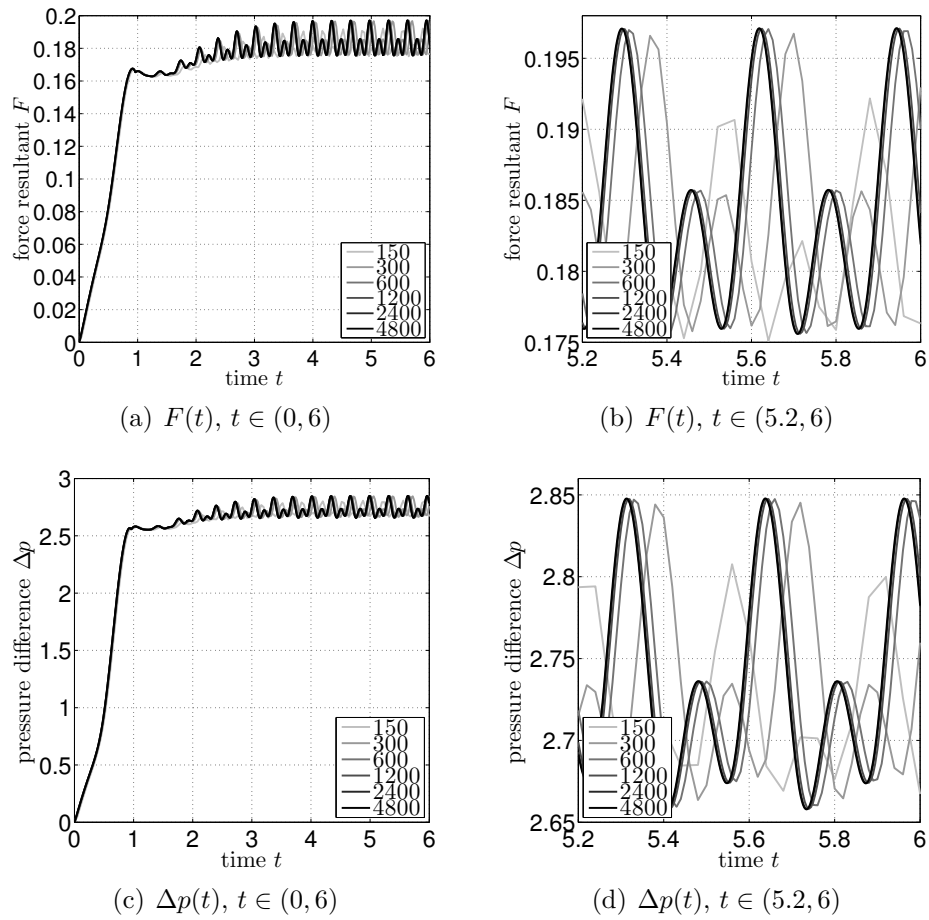


Figure 22: Force resultant $F(t)$ and pressure difference $\Delta p(t)$ obtained on the fine mesh of the cylinder flow test case according to map B.

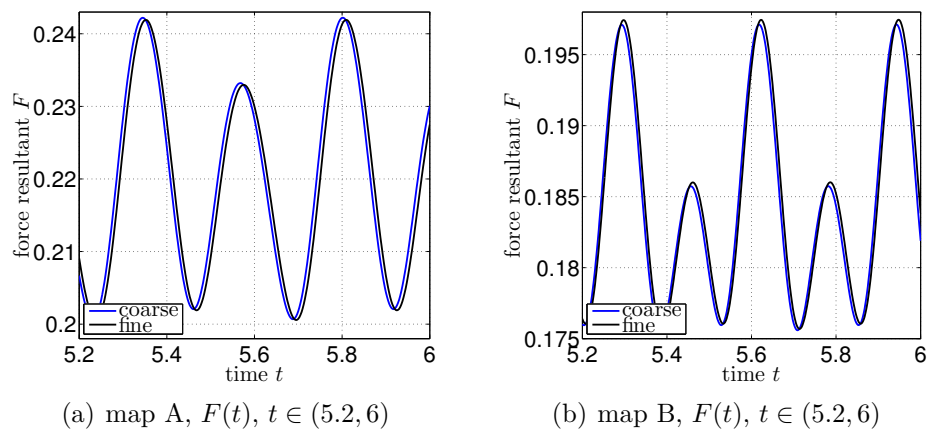


Figure 23: Force resultant $F(t)$ for the cylinder flow test case according to map A and B for the fine and coarse meshes with 4800 time steps.

For the discretization, the surface FEM is employed with quadrilateral or triangular elements. Element spaces of different orders are used for (i) the geometric approximation of the manifold, k_{geom} , (ii) the approximation of the velocity fields, $k_{\mathbf{u}}$, (iii) the pressure field, k_p , and (iv) the Lagrange multiplier field for the enforcement of the tangential velocity constraint, k_λ . The choice of these orders affects the properties of the resulting FEM in terms of conditioning, accuracy, and stability. Particularly useful combinations for a chosen order $k_{\mathbf{u}}$ are $k_{\text{geom}} = k_{\mathbf{u}} + 1$ and $k_p = k_\lambda = k_{\mathbf{u}} - 1$. Some benchmark test cases for flows on manifolds are proposed and higher-order convergence rates are achieved. The notation used in this work is closely related to the engineering literature for the FEM in fluid mechanics. Implementational matters are outlined.

There is a large potential for future research related to this work: One may investigate different stabilization methods such as Galerkin least-squares stabilization and variational multiscale methods. Stabilization may also be useful to circumvent the Babuška-Brezzi condition and enable equal-order shape functions for the velocities and pressure. The tangential velocity constraint may be more efficiently enforced based on penalty methods or other Lagrange multiplier approaches such as the Uzawa method. We believe that flows on manifolds have a strong potential for fundamental research in mathematics, physics, and engineering.

6 Acknowledgements

The fruitful discussions with Dr. Sven Groß, Dr. Thomas Rüber and Prof. Günther Of are gratefully acknowledged.

References

- [1] Babuška, I.: Error-bounds for finite element method. *Numer. Math.*, **16**, 322 – 333, 1971.
- [2] Blaauwendraad, J.; Hoefakker, J.H.: *Structural Shell Analysis*, Vol. 200, *Solid Mechanics and Its Applications*. Springer, Berlin, 2014.
- [3] Bothe, D.; Prüss, J.: On the Two-Phase Navier-Stokes Equations with Boussinesq-Scriven Surface Fluid. *J. math. fluid mech.*, **12**, 133 – 150, 2010.

-
- [4] Brezzi, F.: On the existence, uniqueness and approximation of saddle-point problems arising from Lagrange multipliers. *RAIRO Anal. Numér.*, **R-2**, 129 – 151, 1974.
- [5] Brooks, A.N.; Hughes, T.J.R.: Streamline upwind/Petrov-Galerkin formulations for convection dominated flows with particular emphasis on the incompressible Navier-Stokes equations. *Comp. Methods Appl. Mech. Engrg.*, **32**, 199 – 259, 1982.
- [6] Chan, C.H.; Yoneda, T.: On the stationary Navier-Stokes flow with isotropic streamlines in all latitudes on a sphere or a 2D hyperbolic space. *Dynamics of Partial Differential Equations*, **10**, 209 – 254, 2013.
- [7] Chapelle, D.; Bathe, K.J.: *The Finite Element Analysis of Shells – Fundamentals*. Computational Fluid and Solid Mechanics. Springer, Berlin, 2011.
- [8] Deckelnick, K.; Elliott, C.M.; Ranner, T.: Unfitted finite element methods using bulk meshes for surface partial differential equations. *SIAM J. Numer. Anal.*, **52**, 2137 – 2162, 2014.
- [9] Delfour, M.C.; Zolésio, J.P.: Tangential Differential Equations for Dynamical Thin-Shallow Shells. *Journal of Differential Equations*, **128**, 125 – 167, 1996.
- [10] Delfour, M.C.; Zolésio, J.P.: *Shapes and geometries—Metrics, Analysis, Differential Calculus, and Optimization*. SIAM, Philadelphia, PA, 2011.
- [11] Demlow, A.: Higher-order finite element methods and pointwise error estimates for elliptic problems on surfaces. *SIAM J. Numer. Anal.*, **47**, 805 – 827, 2009.
- [12] Donea, J.; Huerta, A.: *Finite Element Methods for Flow Problems*. John Wiley & Sons, Chichester, 2003.
- [13] Dziuk, G.: *Finite Elements for the Beltrami operator on arbitrary surfaces*, Chapter 6, 142 – 155. Springer Berlin Heidelberg, Berlin, Heidelberg, 1988.
- [14] Dziuk, G.; Elliott, C.M.: Finite element methods for surface PDEs. *Acta Numerica*, **22**, 289 – 396, 2013.
- [15] Ebin, D.G.; Marsden, J.: Groups of diffeomorphisms and the motion of an incompressible fluid. *Ann. of Math. (2)*, **92**, 102 – 163, 1970.

-
- [16] Edwards, D.A.; Brenner, H.; Wasan, D.T.: *Interfacial Transport Processes and Rheology*. Butterworth-Heinemann, Oxford, 1991.
- [17] Franca, L.P.; Hughes, T.J.R.: Two classes of mixed finite element methods. *Comp. Methods Appl. Mech. Engrg.*, **69**, 89 – 129, 1988.
- [18] Fries, T.P.; Omerović, S.: Higher-order accurate integration of implicit geometries. *Internat. J. Numer. Methods Engrg.*, **106**, 323 – 371, 2016.
- [19] Fries, T.P.; Omerović, S.; Schöllhammer, D.; Steidl, J.: Higher-order meshing of implicit geometries—part I: Integration and interpolation in cut elements. *Comp. Methods Appl. Mech. Engrg.*, **313**, 759 – 784, 2017.
- [20] Fries, T.P.; Schöllhammer, D.: Higher-order meshing of implicit geometries—part II: Approximations on manifolds. *Comp. Methods Appl. Mech. Engrg.*, **326**, 270 – 297, 2017.
- [21] Ghia, U.; Ghia, K.N.; Shin, C.T.: High-Re solutions for incompressible flow using the Navier-Stokes equations and a multi-grid method. *J. Comput. Phys.*, **48**, 387 – 411, 1982.
- [22] Grande, J.; Reusken, A.: A Higher Order Finite Element Method for Partial Differential Equations on Surfaces. *SIAM J. Numer. Anal.*, **54**, 388 – 414, 2016.
- [23] Gravemeier, V.: The variational multiscale method for laminar and turbulent flow. *Archives of Computational Methods in Engineering*, **13**, 249, 2006.
- [24] Gresho, P.M.; Sani, R.L.: *Incompressible Flow and the Finite Element Method*, Vol. 1+2. John Wiley & Sons, Chichester, 2000.
- [25] Gross, S.; Reusken, A.: *Numerical Methods for Two-phase Incompressible Flows*, Vol. 40, *Springer Series in Computational Mathematics*. Springer, Berlin, 2011.
- [26] Gurtin, M.E.; Murdoch, I.A.: A continuum theory of elastic material surfaces. *Archive for Rational Mechanics and Analysis*, **57**, 1975.
- [27] Hansbo, A.; Hansbo, P.: A finite element method for the simulation of strong and weak discontinuities in solid mechanics. *Comp. Methods Appl. Mech. Engrg.*, **193**, 3523 – 3540, 2004.

- [28] Hansbo, P.; Larson, M.G.: Finite element modeling of a linear membrane shell problem using tangential differential calculus. *Comp. Methods Appl. Mech. Engrg.*, **270**, 1 – 14, 2014.
- [29] Hughes, T.J.R.; Feijóo, G.R.; Mazzei, L.; Quincy, J.P.: The variational multiscale method—a paradigm for computational mechanics. *Comp. Methods Appl. Mech. Engrg.*, **166**, 3 – 24, 1998.
- [30] Hughes, T.J.R.; Franca, L.P.: A new finite element formulation for computational fluid dynamics: VII. The Stokes problem with various well-posed boundary conditions: symmetric formulations that converge for all velocity/pressure spaces. *Comp. Methods Appl. Mech. Engrg.*, **65**, 85 – 96, 1987.
- [31] Hughes, T.J.R.; Franca, L.P.; Balestra, M.: A new finite element formulation for computational fluid dynamics: V. Circumventing the Babuška-Brezzi condition: a stable Petrov-Galerkin formulation of the Stokes problem accommodating equal-order interpolations. *Comp. Methods Appl. Mech. Engrg.*, **59**, 85 – 99, 1986.
- [32] Hughes, T.J.R.; Franca, L.P.; Hulbert, G.M.: A new finite element formulation for computational fluid dynamics: VIII. The Galerkin/Least-squares method for advective-diffusive equations. *Comp. Methods Appl. Mech. Engrg.*, **73**, 173 – 189, 1989.
- [33] Jankuhn, T.; Olshanskii, M.A.; Reusken, A.: Incompressible fluid problems on embedded surfaces: Modeling and variational formulations. *arXiv:1702.02989*, 2017.
- [34] Khesin, B.; Misiołek, G.: Euler and Navier-Stokes equations on the hyperbolic plane. *Proceedings of the National Academy of Sciences (PNAS)*, **109**, 18324 – 18326, 2012.
- [35] Koba, H.; Liu, C.; Giga, Y.: Energetic variational approaches for incompressible fluid systems on an evolving surface. *Quart. Appl. Math.*, **75**, 359 – 389, 2017.
- [36] Kobayashi, M.H.: On the Navier-Stokes equations on manifolds with curvature. *J. Eng. Math.*, **60**, 55 – 68, 2008.
- [37] Nitschke, I.; Voigt, A.; Wensch, J.: A finite element approach to incompressible two-phase flow on manifolds. *Journal of Fluid Mechanics*, **708**, 418 – 438, 2012.

-
- [38] Olshanskii, M.A.; Reusken, A.; Xu, X.: A stabilized finite element method for advection-diffusion equations on surfaces. *IMA Journal of Numerical Analysis*, **34**(2), 732 – 758, 2014.
- [39] Persson, P.O.; Strang, G.: A Simple Mesh Generator in MATLAB. *SIAM Review*, **46**, 329 – 345, 2004.
- [40] Reusken, A.: Analysis of trace finite element methods for surface partial differential equations. *IMA J Numer Anal*, **35**, 1568 – 1590, 2014.
- [41] Reuther, S.; Voigt, A.: Solving the incompressible surface Navier-Stokes equation by surface finite elements. *Physics of Fluids*, **30**, 012107, 2018.
- [42] Schäfer, M.; Turek, S.: Benchmark Computations of Laminar Flow around a Cylinder. In *Flow Simulation with High-Performance Computers II*. (Hirschel, E.H., Ed.), Vieweg Verlag, Braunschweig, 1996.
- [43] Scriven, L.: Dynamics of a fluid interface equation of motion for Newtonian surface fluids. *Chemical Engineering Science*, **12**, 98 – 108, 1960.
- [44] Shakib, F.; Hughes, T.J.R.; Johan, Z.: A new finite element formulation for computational fluid dynamics: X. The compressible Euler and Navier-Stokes equations. *Comp. Methods Appl. Mech. Engrg.*, **89**, 141 – 219, 1991.
- [45] Slattery, J.C.; Sagis, L.; Oh, E.S.: *Interfacial transport phenomena*, Vol. 2. Springer, Berlin, 2007.
- [46] Taylor, C.; Hood, P.: A Numerical Solution of the Navier-Stokes Equations Using the Finite Element Technique. *Computers & Fluids*, **1**, 73 – 100, 1973.
- [47] Temam, R.: *Infinite dimensional dynamical systems in mechanics and physics*. Springer, Berlin, 1988.
- [48] Tezduyar, T.; Sathe, S.: Stabilization Parameters in SUPG and PSPG Formulations. *J. Comput. Appl. Math.*, **4**, 71 – 88, 2003.
- [49] Tezduyar, T.E.; Osawa, Y.: Finite element stabilization parameters computed from element matrices and vectors. *Comp. Methods Appl. Mech. Engrg.*, **190**, 411 – 430, 2000.